

Dynamic Zoom Simulations of structure formation beyond standard cosmology

Riccardo Zangarelli^{1,2,★}, Marco Baldi^{1,2,3}, Federico Marinacci^{1,2}, Enrico Garaldi^{4,5}

¹ Dipartimento di Fisica e Astronomia “Augusto Righi”, Università di Bologna, via Piero Gobetti 93/2, I-40129 Bologna, Italy.

² INAF, Osservatorio di Astrofisica e Scienza dello Spazio di Bologna, via Piero Gobetti 93/3, I-40129 Bologna, Italy.

³ INFN, Sezione di Bologna, viale Berti Pichat 6/2, I-40127 Bologna, Italy.

⁴ Kavli ITPU (WPI), UTIAS, The University of Tokyo, Kashiwa, Chiba 277-8583, Japan.

⁵ Center for Data-Driven Discovery, Kavli ITPU (WPI), UTIAS, The University of Tokyo, Kashiwa, Chiba 277-8583, Japan.

February 9, 2026

ABSTRACT

Context. A thorough interpretation of the current and upcoming generation of cosmological observations requires unprecedented large-scale, high-resolution simulations spanning multiple cosmological models and parameters. These simulations are extremely computationally demanding, and their realization poses a crucial technical challenge.

Aims. We present beyond- Λ CDM implementations of the Dynamic Zoom Simulations (DZS) method, a performance-enhancing technique tailored for large-scale simulations that produce lightcone-like outputs. This approach dynamically decreases the resolution of a simulation in the regions that are not in causal connection with the observer, substantially saving computational resources without directly affecting the physical properties within the lightcone.

Methods. We implemented the DZS algorithm in two state-of-the-art codes that support non-standard cosmologies, namely modified $f(R)$ gravity in Arepo and dark sector interactions in Gadget4. We then analyzed result accuracy and performance gains across resolution, simulation volume and cosmological model by comparing simulations performed with and without the DZS algorithm.

Results. We show that our DZS reproduce the lightcone halo mass function, sky-projected massmaps, and matter and weak lensing convergence power spectra with an accuracy of $\simeq 0.1\%$ or higher in most cases. In terms of performance, DZS runs in our test simulations can save up to $\sim 50\%$ runtime compared to the non-DZS counterparts. Moreover, scaling our results to larger simulated volumes suggests that performance gains could improve by an additional $\sim 20\%$ at the resolution levels of current state-of-the-art cosmological simulations.

Conclusions. The validation of the DZS algorithm in beyond- Λ CDM models demonstrates that this technique can enable cost-effective, large-scale ($\gtrsim 1$ cGpc/h) simulations with state-of-the-art resolution, providing the computational framework needed to constrain and help the interpretation of forthcoming observational data.

Key words. Cosmology – Methods: numerical – Cosmology: theory – (Cosmology:) dark matter – (Cosmology:) dark energy – (Cosmology:) large-scale structure of Universe

1. Introduction

Cosmological simulations have become a fundamental tool in modern astrophysics. They make it possible to conduct “virtual experiments” on large portions of the Universe, by exploring different cosmologies across various models and parameter spaces. Indeed, the physical processes that shape galaxies and the Large-Scale Structure (LSS) are highly non-linear, which severely limits the applicability of purely analytical approaches and instead requires the use of numerical tools. This means that simulations can be effectively viewed as a theoretical counterpart to real observations (e.g., [Springel 2012](#); [Vogelsberger et al. 2020](#); [Angulo & Hahn 2022](#); [Somerville & Davé 2015](#); [Primack 2024](#)).

Recently, observations are becoming more accurate and deeper than ever thanks to state-of-the-art instruments, such as Euclid ([Laureijs et al. 2011](#); [Euclid Collaboration 2025c](#)), the Vera Rubin Observatory ([Ivezić et al. 2019](#)) and the Dark Energy Spectroscopic Survey ([DESI Collaboration 2016a](#); [2016b](#)), and upcoming ones like the Square Kilometer Array ([Braun et al. 2024](#)).

[2015](#)), Athena ([Nandra et al. 2013](#)), and the Nancy Grace Roman Space Telescope ([Spergel et al. 2015](#)). For a thorough interpretation of this massive amount of data, simulations need to keep up with the unprecedented quality and sky coverage of current observations, providing high-resolution views of wide volumes of the Universe and modeling a large statistical sample of objects with increasing physical fidelity. The latter requirement would ideally imply that the key physical processes driving the formation of observable (luminous) objects – such as gas cooling, star formation, feedback mechanisms (both from stars and active galactic nuclei) and magnetic fields, to name a few – are self-consistently included in a simulation. However, full-physics simulations with a mass resolution $\lesssim 10^9 M_\odot/h$ on Gpc scales are extremely expensive (when feasible at all) with the current generation of high-performance computing facilities, especially when different models or parameters need to be explored through multiple realizations.

A faster and computationally less intensive approach is represented by N -body simulations, coupled with post-processing techniques for galaxy modeling – such as Halo Occupation Distribution model ([Berlind & Weinberg 2002](#)), Subhalo Abundance Matching ([Conroy et al. 2006](#)), and Semi-

* e-mail: riccardo.zangarelli2@unibo.it

Analytical models (Henriques et al. 2015; Somerville et al. 2015; Hirschmann et al. 2016; Lacey et al. 2016). Nevertheless, not even the N -body scenario is free of technical challenges. Hundreds of billions or even trillions of simulation particles (i.e., discrete tracers of the underlying continuous fields) are needed to cover a large, Gpc scale volume with a somewhat high mass resolution ($\lesssim 10^{10} \text{ M}_\odot/h$), resulting in huge memory, storage space and computational requirements. Consequently, it should not come as a surprise that some of the largest simulations to date (e.g., Euclid Flagships I and II, Potter et al. 2017; Euclid Collaboration 2025b; Millennium-XXL, Angulo et al. 2012; DEUS Full Universe, Alimi et al. 2012) have all required millions of core-hours on $\sim 10^4$ computational units.

Moreover, the typical simulation output format (a so-called “snapshot” of the whole volume at fixed cosmic time) does not reflect the survey view of the Universe, as in the latter we receive information from different cosmic times due to the finite value of the speed of light. While a combination of snapshots can mimic this lightcone-like representation – for instance through a piecewise-constant approximation between snapshots adjacent in time – this approach still requires to save to disk and post-process a substantial volume of data, as snapshots can weigh several terabytes each in the most expensive simulations. Therefore, simulations have recently started to switch to an on-the-fly lightcone output approach, either by saving particles in thin shells with radius equal to the light-travel distance R_{lc} (Evrard et al. 2002; Fosalba et al. 2008; Potter et al. 2017), or with more sophisticated lightcone-crossing interpolations of individual particles (Springel et al. 2021). These on-the-fly techniques eliminate the need for a large amount of “traditional” snapshots for large simulations, with the main output now being the lightcone-like one (a few snapshots might still be saved at representative redshifts for further analysis, e.g., on 3D clustering). However, the lightcone output approach does not mitigate the intensive use of computational resources required in modern large-scale cosmological simulations.

This lightcone-like view raises the concern of having an increasingly large fraction of the simulated volume that sits outside of $R_{lc}(t)$: as the latter decreases with increasing time t , more and more particles cross the lightcone and are not in causal connection with the observer anymore. Moreover, at low redshift, the non-linear clustering of matter requires substantially more computational resources than at higher redshifts. The combination of non-linearity and a decreasing R_{lc} implies that eventually most of the computational time and memory available to a simulation will be employed to evolve structures which are discarded from the main output. Therefore, finding a way to reduce the resources used outside of the lightcone represents a logical approach to mitigate the high computational toll taken by state-of-the-art simulations.

A practical implementation of this idea is given by the Shrinking Domain Framework (SDF, Llinares 2017) where the gravitational calculations are only carried out for particles that lie within the lightcone; after a particle crosses it, it is discarded from the simulation. The SDF is very effective in reducing the computational time taken by a simulation, as numerical calculations involve less and less particles with decreasing redshift. However, many gravity solving algorithms in cosmological simulations (including the one employed in Llinares 2017) rely on the periodicity of the simulated volume. Therefore, substantial modifications to the numerical methods are needed for the SDF to produce correct results. Most importantly, it should also be noted that cosmological simulations are typically carried out in within the Newtonian framework of gravity, where changes

in the gravitational potential propagate instantaneously.¹ Consequently, gravitational interactions on scales larger than the lightcone are not modeled self-consistently in simulations adopting the SDF technique.

Due to these shortcomings, it would be preferable to still perform gravitational calculations outside of the lightcone, but at a reduced resolution with respect to the region within R_{lc} . This reduced resolution can be achieved by progressively merging simulation particles outside of the lightcone, to yield more massive discrete tracers that are still part of the simulation (unlike in the SDF). In this way, less computational resources are spent in a simulation, without any major modifications to the N -body solver or significant effects on the main lightcone-like output. This approach, dubbed Dynamic Zoom Simulations (DZS), was originally introduced in the code Gadget3 (based on its predecessor Gadget2 described in Springel 2005) by Garaldi et al. (2020). Their implementation managed to reduce the time taken by a simulation by up to 50%, while retaining 0.1% accuracy, in Λ CDM, dark-matter-only setups. These results indicate that the DZS technique may offer a promising solution to mitigate the technical challenges of the next generation of cosmological simulations. While the Gadget3 implementation was limited to the Λ CDM framework – and therefore did not allow the modeling of alternative cosmologies – our work enables the use of various models across more modern codes.

In this paper, we present upgraded implementations of the DZS technique in the state of the art codes Arepo (Springel 2010; Weinberger et al. 2020) and Gadget4 (Springel et al. 2021) for cosmological models beyond Λ CDM, in order to allow a more performance-friendly analysis of different cosmologies besides the standard one. Specifically, we focus on $f(R)$ modified gravity (MG, implemented in Arepo by Arnold et al. 2019) and dark scattering (DS, originally implemented in Gadget3 by Baldi & Simpson 2015, now available in Gadget4 as well). The paper is structured as follows. A description and physical motivation of these models and their implementations, along with details on the DZS technique, is presented in Section 2. In Section 3, we assess the performance gains of our implementations in dark-matter-only scenarios employing the different cosmological models, as well as their accuracy in reproducing cosmologically relevant output data. Section 4 evaluates the performance of the DZS algorithm in simulations with higher resolution than those used in our limited testing setups. Finally, we present our conclusions in Section 5.

2. Numerical methods and cosmological models

The core idea behind performance enhancement methods such as DZS and the SDF is that when the main output of a large-scale simulation is in the form of a lightcone, the use of computational resources should not be evenly distributed across the simulation volume, but focused mostly on regions that are causally connected to the observer. This concept is depicted graphically in Fig. 1, which is a 1D+1D space-time diagram of an example cosmological simulation, with the spatial dimension on the x axis and the temporal one on the y axis. The observer is placed at point O at redshift zero, and the past lightcone (blue curve) converges towards them from the initial conditions as the simulation

¹ Normally, this approximation yields accurate modeling even of non-linear perturbations, because their scale is well inside the cosmological horizon (equivalently, their velocity is far below the speed of light). Therefore, matter clustering takes place in a non-relativistic regime, which is safe to model with Newtonian dynamics (Chisari & Zaldarriaga 2011).

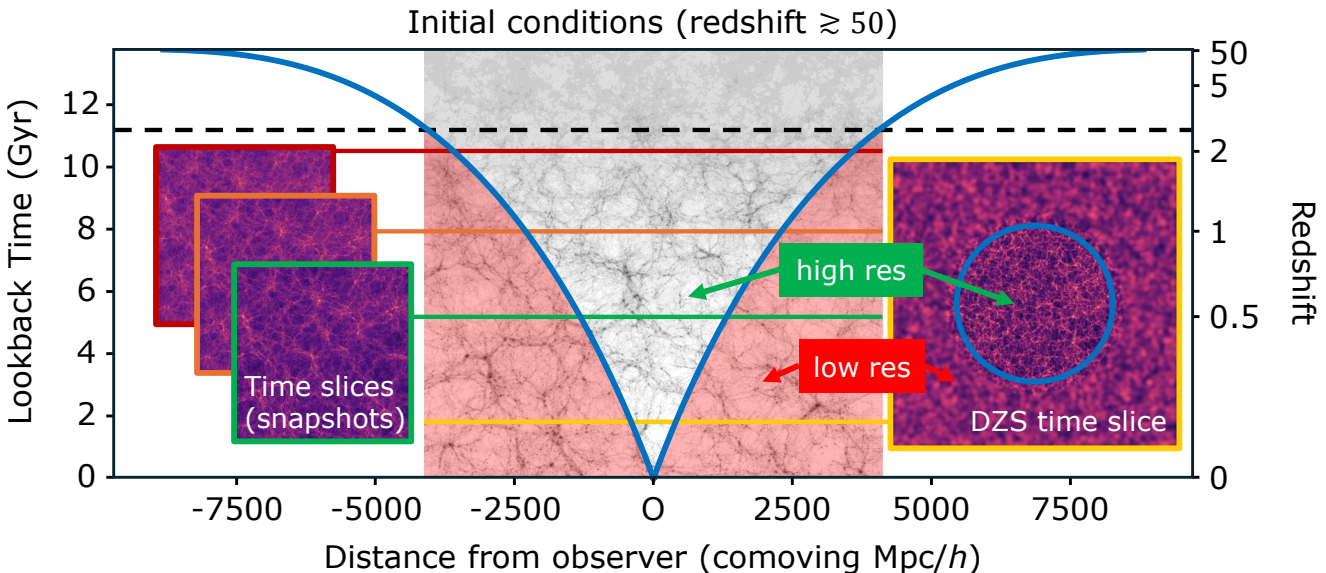


Fig. 1. 1D+1D space-time diagram illustrating the lightcone-like approach of DZS. An example simulation (a cubic box 8192 comoving Mpc/h on a side) is depicted from its initial conditions (top) to redshift, or lookback time, zero (bottom). The depicted density field is only included for displaying purposes, and does not match the size of the volume marked on the x axis (it is rendered from TNG300-3-Dark simulation data, Nelson et al. 2019). The observer is placed at redshift zero at the location marked with O . The simulation volume is crossed by the lightcone (blue curve) at a time indicated by the dashed black line. Traditional snapshots, or “time slices”, are taken at the cosmic times highlighted by horizontal colored lines, leading to fixed-time density maps of real simulation volumes, rendered from the TNG300-3-Dark (left) and the MEDIUM DZS on the right (see Table 1 in Section 3).

progresses. During this process, the lightcone will enter the simulated volume at some redshift z_{lc} , marked by the black dashed line. From z_{lc} onward, an increasingly large fraction of the volume is left out of the lightcone (red shaded area). While traditional snapshots, or “time slices”, include that volume (i.e., the red, orange and green line in Fig. 1 cross the red-shaded area), a lightcone-like output would only consist of the overlap between the blue lightcone curve and the simulation volume. Therefore, the red shaded area can be discarded (as in the SDF) or adjusted on-the-fly to a lower resolution (as in DZS). Time slices can still be extracted to illustrate this procedure, as shown by the yellow line in Fig. 1: the lightcone – marked by a blue circle with radius R_{lc} in the time slice – separates the inner high-resolution area from the outer low-resolution one. This resolution reduction operation in DZS requires only minimal modifications to simulation codes, and no modification to their N -body solver at all (unlike in the SDF). This enables a relatively straightforward implementation of DZS in the majority of cosmological simulation codes, employing both Λ CDM and alternative models. In fact, simulating such models is crucial to interpret survey data: therefore, we implemented and showcase the DZS algorithm also in codes that employ non-standard gravity or exotic dark energy models.

As mentioned in the introduction, a class of non-standard gravity models, the so-called $f(R)$ gravity, was already included in Arepo by Arnold et al. (2019). Therefore, we chose to use this code to test and showcase the capabilities of the DZS algorithm with a non-standard gravitational solver. Moreover, recent results from Lodha et al. (2025) predict significant deviations from the Λ CDM picture through a redshift-dependent equation of state parameter for dark energy $w_{DE}(z)$. For this reason, we also implemented DZS in another code capable of modeling beyond- Λ CDM effects, namely PANDA-Gadget4 (Baldi

& Casalino, in prep.). Among other non-standard scenarios, the code allows to follow dark scattering effects, which take place if $w_{DE} \neq w_{DE,\Lambda\text{CDM}} = -1$.

In what follows, we describe the main features of the two codes adopted in this work and the modeling, scientific motivation and numerical implementations of non-standard, beyond Λ CDM effects. We conclude this methodological section by detailing the key features of DZS implementations in Arepo and Gadget4.

2.1. Arepo

Arepo is a N -body and galaxy formation code, first presented in Springel (2010) and publicly released in Weinberger et al. (2020). It is massively parallel and employs the Message Passing Interface (MPI, Message Passing Interface Forum 1993), making it suited for state-of-the-art simulations distributed over a large number of computational units. Examples of these include the IllustrisTNG suite (Nelson et al. 2019) and the MillenniumTNG project (Pakmor et al. 2023).

Arepo follows the evolution of discrete mass tracers that interact gravitationally and, if gas is included, hydro-dynamically. Hybrid numerical schemes are used for both types of interactions, with a treePM algorithm handling gravity and a moving Voronoi mesh for hydrodynamics. Our current implementation of DZS in Arepo supports N -body, collisionless simulations, so we focus only on the numerical treatment of gravitational interactions. We refer the interested reader to Springel (2010) and Weinberger et al. (2020) for further details on the moving mesh approach.

The treePM scheme (Xu 1995; Bode et al. 2000; Bagla 2002) combines the particle-mesh method (PM, e.g., Klypin & Shandarin 1983), to compute long-range interac-

tions, with the hierarchical multipole method (or “tree” method, Barnes & Hut 1986) for short-range forces. In the following we briefly describe the implementation of the gravity tree, since it is crucial for both the DZS algorithm and the $f(R)$ gravity implementation described below.

The tree method approximates the contributions of distant groups of particles (the so-called “nodes” of the tree) through their multipole expansion, deciding which nodes are distant enough through a “geometrical” criterion – although other, not distance based, criteria exist. The tree construction algorithm splits the cubic simulation domain, called “root node”, into eight equal-volume subdomains, which are the “children” nodes of the root node. Each child node is again split into eight subdomains, and the process continues recursively until the smaller nodes contain at most one simulation particle. This ensures that the tree naturally adapts to the gravity-driven clustering of particles, creating increasingly smaller nodes. Each node built during this construction process stores the mass and center of mass of its particle content (used to calculate multipole moments), as well as links to other nodes (i.e., its “father”, “siblings” and “children”). We anticipate that this tree structure can be employed by DZS to reduce the simulation resolution outside of the lightcone, because the properties of a node, i.e., quantities evaluated over its particle content, provide a straightforward way to merge those particles into more massive, and therefore lower-resolution, tracers. Furthermore, the presence of multiple, nested grids in the structure of the tree makes it well suited to be directly employed in multi-grid solvers, such as the one used by Arnold et al. (2019) to calculate modified gravity contributions to particle interactions.

2.1.1. $f(R)$ gravity in Arepo

The use of General Relativity (GR) as a description of gravity is a fundamental assumption of the standard cosmological model. Several small-scale experimental tests agree with the predictions of GR up to high levels of precision (Will 2014). Nonetheless, on scales larger than our Solar System GR remains largely unconstrained. For this reason, generalizations of GR that only influence cosmological scales (employing “screening” mechanisms to ensure that GR predictions are restored in high-density environments, where these have been tightly constrained) represent an interesting approach to achieve a better understanding of the nature of gravity and its role in the cosmic accelerated expansion and the evolution of the LSS. This type of investigations is particularly timely in view of forthcoming large-scale tests of gravity, enabled by precise measurements of object clustering from missions such as Euclid (Laureijs et al. 2011; Euclid Collaboration 2025c).

Among these generalizations, we focus on $f(R)$ gravity, where the Einstein field equations of GR are modified through a function f of the Ricci scalar R . Specifically, we consider a class of $f(R)$ models that can account for the accelerated expansion of the Universe without needing a cosmological constant Λ (Hu & Sawicki 2007). In the Newtonian approximation commonly employed in cosmological simulations, including $f(R)$ gravity effects yields a modified Poisson equation of the form

$$\nabla^2 \Phi = \frac{16\pi G}{3} \delta \rho - \frac{1}{6} \delta R, \quad (1)$$

where Φ is the gravitational potential, G is the gravitational constant, and $\delta \rho$ and δR are perturbations in the matter density and

scalar curvature, respectively. The latter can be conveniently expressed in terms of $f_R \equiv df(R)/dR$, which represents the scalar field responsible for beyond-GR effects. The approximated field equation for f_R is (e.g., Oyaizu 2008):

$$\nabla^2 f_R = \frac{1}{3} (\delta R - 8\pi G \delta \rho). \quad (2)$$

Combining eq. (1) and (2), the modification to standard gravity can be expressed in terms of an additional acceleration \mathbf{a}_{MG} experienced by a particle:

$$\mathbf{a}_{MG} = \frac{c^2}{2} \nabla f_R, \quad (3)$$

which can be computed by solving eq. (2). This additional contribution to gravitational interaction enhances them up to a factor of 4/3. It can be shown (Puchwein et al. 2013; Arnold et al. 2019) that the $f(R)$ gravity models by Hu & Sawicki (2007) can be effectively parametrized by \bar{f}_{R0} , i.e., the mean value of f_R at redshift zero. Since these models are derived from a general broken power-law parametrization, its exponent n is also needed to describe them. Nonetheless, most studies, including Arnold et al. (2019), set $n = 1$.

A computational treatment of $f(R)$ gravity has the main task of solving numerically eq. (2). The implementation of Arnold et al. (2019) in Arepo (dubbed MG-Arepo) closely follows the MG-Gadget project of Puchwein et al. (2013): in both cases, the oct-tree from the tree N-body solver is used as an adaptive grid to solve a discretized version of eq. (2)². This discretized version, however, is highly non linear, requiring the use of multi-grid iterative solvers. Nonetheless, even with the use of a multi-grid technique, the $f(R)$ solver leads to a substantial increase in computing time in Arepo simulations with respect to a Λ CDM setup: this increase amounts to a factor of 2 or more for setups analyzed in this work, but it can very well exceed one order of magnitude for higher-resolution runs (e.g., Appendix A in Euclid Collaboration 2025a). This makes MG-Arepo the ideal example of a computationally heavy N -body framework that can benefit from performance gains brought by the DZS algorithm (see Section 3 for details).

As a final remark, we would like to note that the version of MG-Arepo presented in Arnold et al. (2019) does not include lightcone output capabilities, which are a key element of DZS. We added this crucial feature by porting into MG-Arepo the Gadget4 implementation of the lightcone output mode described in Springel et al. (2021).

2.2. Gadget4

Gadget4 (Springel et al. 2021) is a N -body and galaxy formation code which shares many similarities with Arepo in the handling of gravitational interactions, as it also employs the treePM scheme (generally with the same workflow described in Section 2.1). Hydrodynamics, on the other hand, is modeled through the Smoothed Particle Hydrodynamics (SPH) approach. We refer to Springel et al. (2021) for details on the SPH technique.

As well as Arepo and many other massively parallel codes, Gadget4 also adopts MPI as the parallelization framework, albeit in a hybrid shared-distributed memory variant. We will see in Appendix B that this detail is needed to understand the performance of our Gadget4 simulations.

² The main difference between the two codes lies in a different parametrization to express a discretized version of eq. (2), although MG-Arepo reaches higher accuracy.

2.2.1. Dark scattering in Gadget4

Findings from [Lodha et al. \(2025\)](#) suggest a significant deviation of the dark energy equation of state from the time-independent behavior prescribed by Λ CDM. Coupled with our little understanding of the physical nature of dark matter and dark energy (the so-called “dark sector”), this leaves ample room for speculations about the physical framework that drives the evolution of these components. While a similar line of reasoning with respect to constraints on GR leads to the formulation of modified gravity theories (see Section 2.1.1), a hypothetical interaction between the dark sector components might very well be non-gravitational (e.g., [Wetterich 1995](#); [Amendola 2000](#); [Farrar & Peebles 2004](#)). In fact, the exchange of momentum and energy between dark matter and dark energy can also alleviate cosmological tensions, for example between early and late measurements of the clustering of matter (e.g., [Pourtsidou & Tram 2016](#); [Baldi & Simpson 2017](#)).

In this work, we focus on pure momentum exchange between dark matter and dark energy, i.e., an interaction akin to an elastic scattering. When modeling the dark sector components as a fluid, the exchange arises as an additional “drag” term $A(z)$ in the momentum equation, of the form (e.g., [Simpson 2010](#); [Baldi & Simpson 2017](#); [Cruickshank et al. 2025](#))

$$A(z) \equiv (1 + w_{DE}) \frac{\sigma}{m_{CDM}} \frac{3\Omega_{DE}(z)}{8\pi G} H(z), \quad (4)$$

where σ is the scattering cross section, m_{CDM} is the mass of a cold dark matter particle (throughout this paper we will use $\sigma/m_{CDM} = 100 \text{ cm}^2/\text{GeV}$), Ω_{DE} is the dark energy density parameter, and $H(z)$ is the Hubble parameter. It is now clear that $A \neq 0$ only if $w_{DE} \neq -1$, that is, a non-standard evolution of dark energy. We chose to adopt DESI-inferred trends for $w_{DE}(z)$, using the best-fit (DESI+CMB+Union3) values from [Abdul Karim et al. \(2025\)](#), namely a Chevallier-Polanski-Linder (CPL) parametrization $w_{DE}(z) = w_0 + w_a z/(1+z)$ with $w_0 = -0.667$, $w_a = -1.09$. This $w_{DE}(z)$ is plotted in Fig. 2 (blue curve). Notably, this parametrization exhibits “phantom crossing”, that is, $w_{DE} < -1$ at high z . Both the transition into this “phantom regime” and the regime itself pose serious theoretical challenges (e.g., [Carroll et al. 2003](#); [Vikman 2005](#)); therefore, we also employ a so-called “thawing” parametrization, where w_{DE} is “locked” at -1 at high z and is then allowed to move in the non-phantom regime ($w_{DE} \geq -1$) at lower redshifts. We adopt the parameterization in [Lodha et al. \(2025\)](#), their eq. 15) and choose $p = 4$ to mimic the low- z behavior of the best DESI+CMB+Union3 fit (as seen in the orange curve of Fig. 2). In accordance to the thawing behavior, in this case we chose $w_a = -0.333$ (w_a appears in [Lodha et al. 2025](#), their eq. 15), so that $w_0 + w_a = -1$.

The numerical implementation of dark scattering in Gadget4 is relatively straightforward. We employ the PANDA-Gadget4 framework (Baldi & Casalino, in prep.), which reads tabulated values for $w_{DE}(z)$, $\Omega_{DE}(z)$, $\Omega_M(z)$ and $H(z)$ and uses them to calculate $A(z)$, which then yields the dark scattering contribution to the acceleration of tracer DM particles. Unlike in MG-Arepo, the computational toll of this additional interaction is essentially negligible. However, in our DZS showcase framework, PANDA-Gadget4 proves that even when the non-standard calculations are computationally light, DZS can still yield significant performance improvements (as shown in Section 3.4).

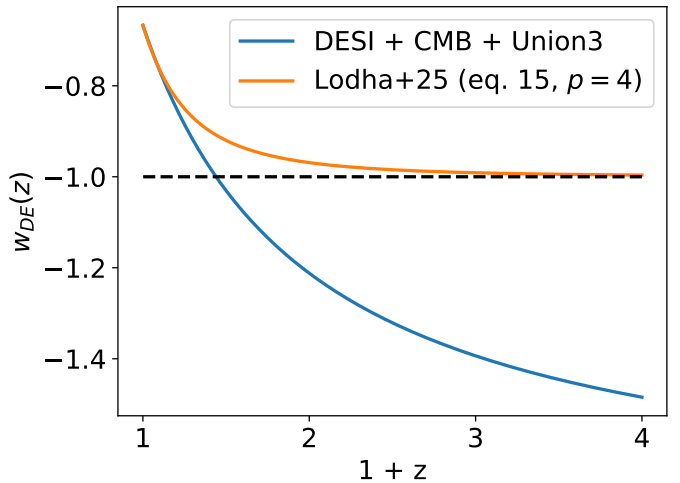


Fig. 2. Equation of state (EoS) parameter of dark energy w_{DE} as a function of redshift z . The blue curve is the best-fit CPL parametrization from [Abdul Karim et al. \(2025\)](#), with $w_0 = -0.667$, $w_a = -1.09$. Its “phantom” behavior ($w_{DE} < -1$) at high z is highlighted by the dashed black line, which marks $w_{DE} = -1$. The orange curve represents a thawing EoS (characterized by $w_{DE} \rightarrow -1$ for $z \rightarrow +\infty$) taken from [Lodha et al. \(2025\)](#), their eq. 15), and reproducing the low- z trend of the CPL best-fit without the phantom behavior.

2.3. The Dynamic Zoom Simulations algorithm

The practical implementation of DZS in both MG-Arepo and PANDA-Gadget4 builds on top of the oct-tree structure. The tree nodes contain the integrated physical quantities of their particle content, such as mass and center of mass. In fact, the gravitational approximation employed by the tree treats nodes as if they were a single “fictitious” particle, holding the combined mass of the particles inside the node and located in its center of mass. In the DZS algorithm, the nodes fulfilling a “derefinement” criterion are converted into actual particles and their particle content eliminated. In other words, when a tree node can be de-refined, DZS replaces its particle content with the corresponding single “fictitious” particle, which is then turned into a real mass tracer.

More specifically, DZS operates from a redshift z_{lc} , at which the lightcone enters the volume of a simulation, by performing the following tasks in any global discrete timestep:³

- calculate the value of R_{lc} at the current step;
- perform a depth-first “tree walk” (akin to the one done by the tree solver and detailed in [Garaldi et al. 2020](#)) to check if nodes outside of the lightcone can be merged into a particle, according to a user-defined derefinement criterion. Those nodes are flagged for derefinement and the particles they contain are flagged for elimination;
- remove from the simulation the particles flagged for elimination;
- use the mass, center of mass and center of mass velocity of flagged nodes to create new low-resolution particles to replace the ones that have been removed.

Repeating these operations over and over as the simulation advances yields a progressively reduced number of particles, as

³ Both Arepo and Gadget4 employ discrete timesteps to advance the trajectories of simulated particles. Each particle is allowed to have its own timestep (e.g., for an accurate integration of high-density environments). DZS can operate only when all particles adjust to the same simulation time, i.e., “synchronize”. This happens in so-called “global” timesteps.

most of the simulation volume adjusts to a lower resolution. This results in decreased memory and run time requirements, without significant modifications to the lightcone-like output.

Besides the tree itself, the derefinement criterion employed in DZS can also be borrowed from the hierarchical multipole solver. In fact, the DZS adaptation of the geometric criterion tests the distance between a node located outside of the lightcone and the "outer edge" of the lightcone itself, i.e., the spherical surface with radius R_{lc} . If the node is far enough from the lightcone edge, it satisfies the criterion and is flagged for derefinement. More specifically, when

$$\frac{L}{|s| - (R_{lc} + b)} < \theta_{geom} \quad (5)$$

a node is flagged and its particles are merged. Here, θ_{geom} is a user-defined threshold, L is the linear size of a node, s is the position of its center of mass with respect to the observer, and b is a user-defined "buffer length" which keeps an additional volume beyond the lightcone at the original simulation resolution. This length ensures that at $z = 0$ (where $R_{lc} = 0$) a sphere with radius b is kept at the original simulation resolution. Note that eq. (5) only applies to nodes outside of the lightcone, for which $|s| > R_{lc} + b$. More generally, a user-tweakable derefinement criterion enables a gradual transition between the original and lower resolution, minimizing the impact of DZS on the dynamics of particles inside the lightcone and giving the user a high degree of control over DZS performance and accuracy. In all the simulations analyzed in this work, we set $\theta_{geom} = 0.1$ and $b = 5r_{mean}$, with $r_{mean} \equiv L_{box}/(N_{part})^{1/3}$ being the mean interparticle separation, L_{box} the side of the cubic simulation volume and N_{part} the initial number of particles. These values are the default parameters set by [Garaldi et al. \(2020\)](#), which we also employ for comparison purposes.

Finally, we would like to remind the reader that the gravitational framework of cosmological simulations is often Newtonian, and this is also the case in our Arepo and Gadget4 simulations. The resulting instantaneous propagation of gravitational interactions implies that the reduced resolution outside R_{lc} affects, to some extent, the contents of the lightcone as well. More specifically, the large-scale gravitational field needs to be preserved for DZS to be reasonably accurate. We ensure this by setting a maximum size L_{max} for nodes that can be derefined, regulating the minimum resolution outside the lightcone so that it is not too low (see also [Garaldi et al. 2020](#)). We use the default value of the maximum linear size of a node $L_{max} = 4r_{mean}$, which roughly translates to a minimum mass resolution 64 times coarser than it would be without derefinement.

For the sake of brevity, we only provided a somewhat general, albeit self-consistent, description of how the practical implementation of the DZS algorithm works and what are its user-defined parameters. While there are some technical differences between our implementations and the original Gadget3 one, most of the details extensively discussed in [Garaldi et al. \(2020\)](#) remain basically unchanged. Therefore, we refer the reader to that work for further details.

3. DZS algorithm validation

We now showcase our DZS implementations in terms of accuracy (i.e., the ability to reproduce cosmologically relevant observables) and performance gains on the wall-clock time taken by simulations. To this end, for a given set of initial conditions (all created with the Multi-Scale Initial Conditions tool, MUSIC, [Hahn & Abel 2011](#)), we performed two simulations: one

Table 1. Simulation parameters used for algorithm validation, including the side length of the simulated volume, the number of simulation particles, the resulting mass resolution, and the redshift range in which lightcone output was produced. The latter is chosen to ensure that $R_{lc}(z) < L_{box}/2$ always, avoiding any box replications. Note that, at the highest considered redshifts, the DZS algorithm has already significantly modified the simulation volume.

name	L_{box} [cMpc/h]	N_{part}	mass res [M_{\odot}/h]	lightcone z range
MEDIUM	2048	512 ³	5.53×10^{12}	[~ 0.36, 0]
MEDIUMHR	2048	1024 ³	6.91×10^{11}	[~ 0.36, 0]
LARGE	8192	512 ³	3.54×10^{14}	[~ 2.5, 0]
LARGEHR	8192	1024 ³	4.42×10^{13}	[~ 2.5, 0]

with the DZS algorithm enabled (dzs hereafter) and one without it (std hereafter). We refer to such a pair as "twin" simulations. We employed volume and particle configurations similar to those found in [Llinares \(2017\)](#) and [Garaldi et al. \(2020\)](#), adapted to our range of different models and parameters, as well as to our available computational resources. Cosmological parameters were set to Planck 2018 values ([Planck Collaboration 2020](#)), that is, $\Omega_{DE} = 0.6889$, $\Omega_M = 0.3111$, and $H_0 = 67.66 \text{ km s}^{-1} \text{ Mpc}^{-1}$. We list our initial condition setups in Table 1.

We carried out our validation for a range of cosmological models: for MG-Arepo, we used two values for \bar{f}_{R0} , i.e., -10^{-5} and -10^{-6} . The former yields a stronger scalar field with more prominent modified gravity effects,⁴ while the latter is closer to the Λ CDM case. For dark scattering simulations with PANDA-Gadget, we employed the two $w_{DE}(z)$ parameterizations shown in Fig. 2, namely the [Abdul Karim et al. \(2025\)](#) best-fit and [Lodha et al. \(2025\)](#) thawing parametrization. As a reference, we also include Λ CDM runs performed with Arepo. Employed models are summarized in Table 2. For each configuration, we performed a twin pair of simulations with every setup outlined in Table 1. This amounts to a total of 40 simulations, which would have been unfeasible to carry out with resolutions higher than our fiducial MEDIUMHR. Based on these results, we nonetheless provide an approximate analysis for higher-resolution performance in Section 4.

Our validation started with an accuracy assessment on the output of twin simulations. We chose to focus on the output that the DZS method is tailored to produce, i.e., lightcone-like output. This is because the heavy modifications introduced by the DZS method on the simulation domain (i.e., a substantial change in resolution and reduction of the total number of particles) prevent 3D power spectra or halo mass functions from being readily calculated. Note that our analysis is strongly dependent on the chosen parameters for DZS, namely the buffer zone b , opening angle θ_{geom} and especially maximum node size to be merged L_{max} , which controls the accuracy of the large-scale gravitational field. The DZS algorithm can be made arbitrarily accurate (e.g., by lowering θ_{geom} for a stricter derefinement criterion), at the cost of a reduced performance boost. We refer to [Garaldi et al. \(2020\)](#) for an extensive parameter variation analysis.

⁴ In fact, such a value for \bar{f}_{R0} is in tension with observations (e.g., [Arnold et al. 2019](#)); nonetheless, it is a standard parameter choice for simulations of modified gravity (e.g., [Winther et al. 2015](#)), yielding clearly identifiable effects both in force enhancement and screening (e.g., [Hagstotz et al. 2019](#)).

Table 2. Models and parameters adopted in the DZS algorithm validation.

Model name	Model ref.	Parameters	Code
Λ CDM	n.n.	n.n.	Arepo
MG-F5	Arnold et al. (2019)	$\tilde{f}_{R0} = -10^{-5}$	MG-Arepo
MG-F6	Arnold et al. (2019)	$\tilde{f}_{R0} = -10^{-6}$	MG-Arepo
DS-DESI	Abdul Karim et al. (2025)	CPL, $w_0 = -0.667, w_a = -1.09$	PANDA-Gadget4
DS-THAW	Lodha et al. (2025)	their eq. 15, $w_0 = -0.667, w_a = -0.333, p = 4$	PANDA-Gadget4

3.1. Lightcone halo mass function

The lightcone halo mass function (LCHMF) represents the number density of dark matter halos as a function of their mass, in a lightcone-like view over a certain redshift range. Arepo and Gadget4 employ the Friends-of-Friends (FoF) algorithm (Davis et al. 1985) for detecting collapsed structures from a distribution of particles. In our case, this distribution is made of the interpolated positions of particles crossing R_{lc} (i.e., the main lightcone output), which we ran through the FoF algorithm in postprocessing to detect halos directly on the lightcone. The resulting halo masses were then binned on an arbitrary number of 21 bins between 10^{13} and $10^{15} \text{ M}_\odot/h$. Due to the limited resolution of our validation suite (Table 1), we computed the LCHMF only for the MEDIUMHR simulations. While these simulations yield only the top end of the LCHMF, we are still able to cover ~ 2 orders of magnitude.

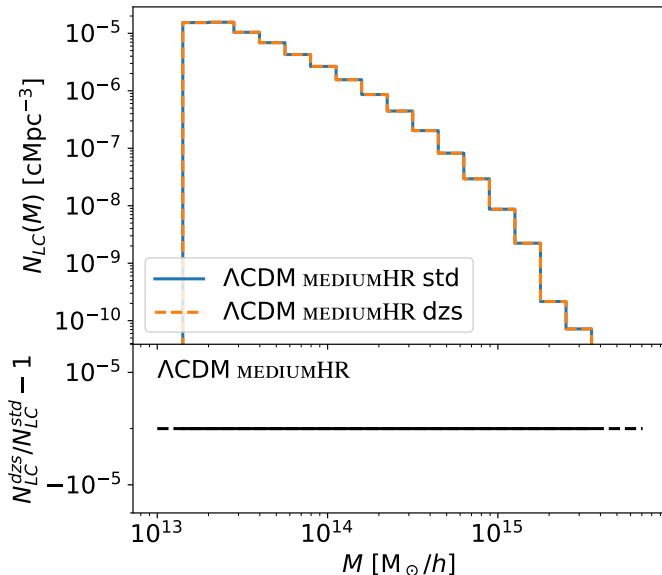


Fig. 3. Lightcone halo mass function of the Λ CDM MEDIUMHR twin simulations (top). The std solid histogram and the dzs dashed histogram are in excellent agreement. This is also shown by the relative difference plot between the two curves (bottom), where we arbitrarily set the y axis scale.

We show the LCHMF for the twin MEDIUMHR Λ CDM simulations in Fig. 3. The std simulation is reproduced exactly by the corresponding DZS run. The non-standard cases are depicted in Fig. 4. The MG-F5 model yields relative differences of $\sim 2\%$ at most between the dzs and std simulations, at the highest masses where only a handful of halos are detected (middle left panel of Fig. 3). On the other hand, the MG-F6 model is very similar to the Λ CDM scenario, only showing $\sim 0.001\%$

differences in halos with masses around $10^{14} \text{ M}_\odot/h$. The DS-DESI and DS-THAW models also show minimal differences, with the former always remaining below 0.01% and the latter peaking at $\sim 0.1\%$. With the DZS algorithm, we were also able to retrieve physical signatures of the different cosmologies. The MG-F5 model (solid blue and dashed orange lines in the top left panel) shows an increased density of halos with respect to the reference Λ CDM case (as expected from the enhanced gravity of the $f(R)$ framework). The MG-F6 setup, where modified gravity produces weaker effects, remains closer to the reference model. The dark scattering models show interesting LCHMF trends with respect to Λ CDM, with the DS-THAW model (solid green and dashed red lines in the top right panel of Fig. 4) having a lower number density of halos than the standard case, due to the factor $A(z)$ being always > 0 (see eq. 4). For the DS-DESI case, $A(z) < 0$ in the phantom regime, resulting in a shift of collapsed halos towards high masses. We conclude that DZS reproduce the LCHMF of our highest resolution setup with high accuracy in all of the examined non-standard cosmologies, with the highest relative difference being $\sim 2\%$ in the MG-F5 model at the largest halo masses ($\gtrsim 5 \times 10^{14} \text{ M}_\odot/h$). Note that a larger halo statistics might very well improve this result.

3.2. Sky-projected lightcone and angular power spectrum

In addition to the 3D distribution of lightcone-crossing particles employed in the LCHMF calculation, the on-the-fly lightcone output capabilities also allow to save a sky-projected HEALPix (Górski et al. 2005) pixelization of those particles. We compared the resulting angular matter density maps to assess pixel-scale relative differences, and examined angular power spectra of matter clustering. We created density maps for the MEDIUMHR simulation, which has the highest resolution in the validation suite, and computed power spectra for the MEDIUMHR, MEDIUM and LARGEHR simulations. We used a value $\text{NSIDE} = 1024$ for our HEALPix output,⁵ resulting in a maximum multipole moment $l \simeq 3000$ in the power spectra. We averaged the value of each moment across 80 logarithmically spaced bins. Angular matter density maps were downsampled to $\text{NSIDE} = 256$ for visual clarity.

Figure 5 shows the angular matter density (labeled as Σ) maps of the MEDIUMHR twin simulations, run with the Λ CDM, MG-F5 and DS-DESI models. The Λ CDM and DS-DESI maps are almost identical in the std and dzs case, having only a few “outlier” pixels with non-zero relative difference of 1% at most in absolute value. On the other hand, the MG-F5 result is noticeably different. This is due to the MG contribution being calculated at node level (that is, on each cell of the multi-grid solver),

⁵ In a HEALPix pixelization, NSIDE represents the number of pixels per side, and relates to the total number of pixels in a map NPIX as $\text{NPIX} = 12 \times \text{NSIDE}^2$.

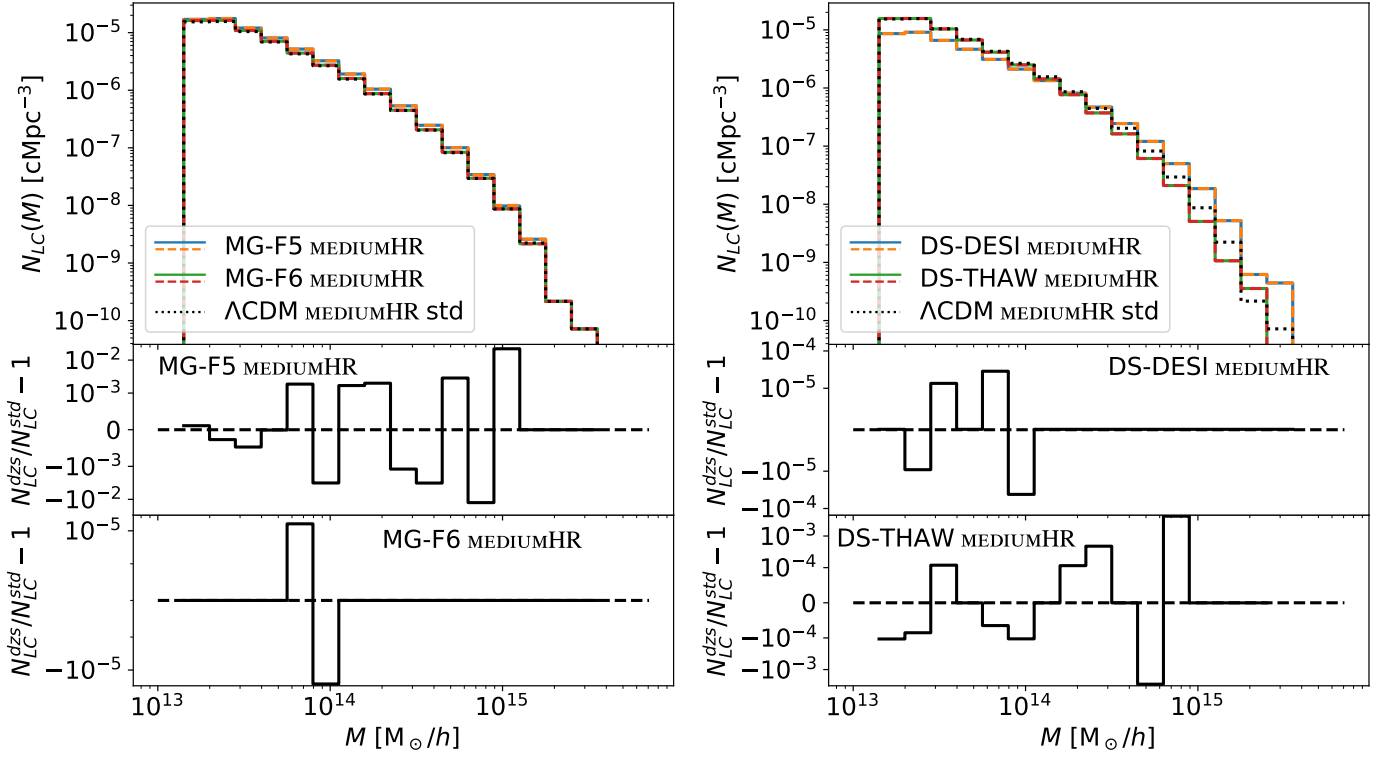


Fig. 4. *Left column:* Lightcone halo mass function of the MG-Arepo MEDIUMHR twin simulations, for the MG-F5 and MG-F6 models (top panel). Solid lines refer to std runs, dashed lines to dzs ones. The ΛCDM std case is overlaid as a dotted line for reference. Relative difference plots are included for both MG models (middle and bottom panels), with a dashed line at $N_{LC}^{\text{dzs}}/N_{LC}^{\text{std}} - 1 = 0$ for reference. *Right column:* the same as in the left column, but for the DS-DESI and DS-THAW MEDIUMHR simulations.

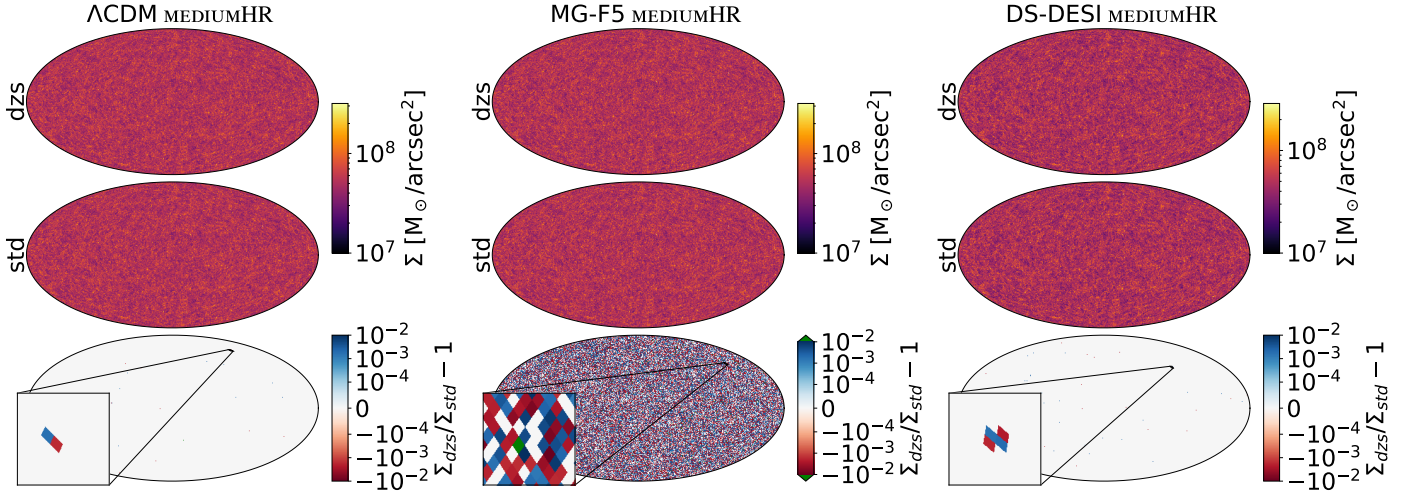


Fig. 5. Maps showing the angular matter density Σ of the MEDIUMHR twin simulations in the ΛCDM (left column), the MG-F5 (middle column) and the DS-DESI (right column) cases. For each of the three models, maps for the dzs and std simulations are depicted in the top and middle panel, respectively. At the bottom, the relative differences between the dzs and std cases are shown, with the MG-F5 case employing the color green for differences above 1% in absolute value.

and then mapped to the particles in each node. The extremely small positional displacements induced by DZS in the particle distribution (even of the order of one-billionth of the spatial resolution) can move particles from one node to another – or prevent the creation of finer grid cells altogether – and yield different MG contributions at particle level. The fact that these differences arise within the lightcone leads to faster-propagating and more significant changes in the output. Nonetheless, as shown in Fig. 5, the accuracy is still at percent level at worst, and only a

small fraction of pixels (0.9% of the total, highlighted in green) yields differences greater than 1% in absolute value.

Figure 6 depicts the matter power spectrum for the ΛCDM MEDIUMHR, MEDIUM and LARGEHR twin simulations (due to their low resolution, the LARGE simulations are not included and will only be used for performance estimation). Pairs of solid lines (std simulations) and dashed lines (dzs simulations) refer to different setups. Due to the broader redshift range of the lightcone output in the LARGEHR runs, which encompasses structures

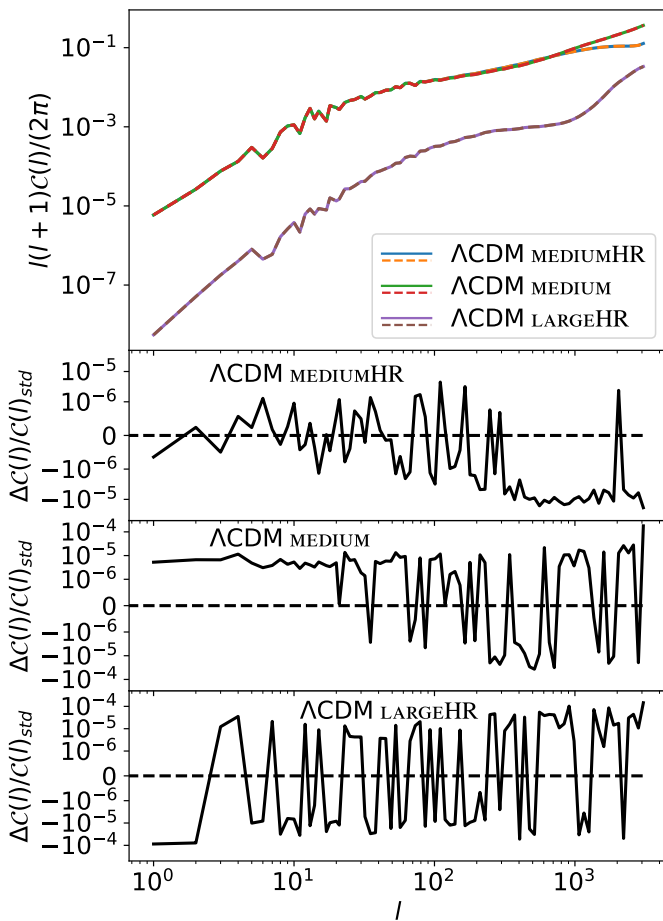


Fig. 6. Top panel: Angular power spectrum $C(l)$ of Λ CDM MEDIUMHR, MEDIUM and LARGEHR runs. The power is lower in the latter pair of simulations due to the larger output redshift range (see Table 1). Solid lines refer to std runs, dashed lines to dzs ones. Bottom panels: Relative differences between the dzs and std simulations for the different run types discussed above, as indicated in each panel. The dashed line is located at $\Delta C(l) = 0$ as a reference.

at higher z than the MEDIUM and MEDIUMHR boxes (akin to a “deeper survey”), the density contrast is less pronounced and the power is significantly lower. As for the MEDIUM and MEDIUMHR simulations, the same box at a different resolution yields visually identical results with the exception of the smallest scales (largest l) sampled, where the lower resolution shows a higher power. The accuracy of the DZS algorithm is very high in the Λ CDM framework: solid and dashed lines look exactly the same to the naked eye, and the relative difference plots (bottom panels in Fig. 6) confirm this trend. Differences sit at $\sim 0.01\%$ at worst in the LARGEHR and MEDIUM setups. Note that the latter is outperformed in accuracy by its higher-resolution counterpart: this trend is very promising for the use of the DZS algorithm in state-of-the-art, high-resolution cosmological simulations. Finally, for the sake of completeness, we note that the MEDIUMHR runs show seemingly non-random differences at small scales, with the dzs simulation having slightly ($\sim 0.001\%$) less power. Since this difference is so small, we did not investigate it further.

The beyond- Λ CDM cases are shown in Fig. 7 for the MEDIUMHR simulations. As it was the case in the LCHMF comparison, the MG-F5 MEDIUMHR simulations (solid blue and dashed orange lines in the top left panel of Fig. 7) yield the worst results among our validation setups (as shown by the relative differences

in the middle left panel of the same figure). Nonetheless, relative differences remain around 0.01% for most values of l , only rising to 0.1% at the lower end of the sampled scales, corresponding to $l \gtrsim 10^3$. The power spectrum itself also shows a boost with respect to the reference Λ CDM case, in accordance with the LCHMF (Fig. 4) and the theoretical $f(R)$ framework. The MG-F6 MEDIUMHR simulations, instead, are more similar to the standard setup both in power spectrum boost (solid green and dashed red line in the top left panel of Fig. 7) and relative differences (bottom left panel of the same figure). The PANDA-Gadget4 MEDIUMHR simulations (top right panel of Fig. 7), are also consistent with their LCHMF: the DS-DESI model is boosted at larger scales and suppressed at smaller scales with respect to Λ CDM, whereas the thawing model (DS-THAW) has slightly less power for most values of l . The comparison between std and dzs runs (middle right and bottom right panel of Fig. 7) yields extremely small, visually random differences. Specifically, these remain below $\sim 0.001\%$, except for $l \gtrsim 10^3$ in the DS-THAW model, for which differences increase by approximately one order of magnitude.

We include additional figures, containing the power spectra of the non-standard MEDIUM and LARGEHR simulations, in Appendix A (Figs. A.1 and A.2). Here, we remark that the DZS-induced differences are very contained in those setups as well. Furthermore, a comparison between the MEDIUM and the MEDIUMHR runs shows that, unlike the standard setup of Fig. 6, the differences in some models (namely MG-F5 and DS-THAW) do not improve with resolution; we note, however, that they do not get worse either. We expect this behavior to continue in the high-resolution, large-scale scenarios that the DZS algorithm is tailored for. More generally, we note that all of the relative differences depicted in Figs. 6, 7, A.1 and A.2 are well within the accuracy required for modern (i.e., “Stage-IV”) surveys. For the Euclid mission, for example, Laureijs et al. (2011) and Euclid Collaboration (2020) indicate a 1% accuracy forecast for matter power spectrum measurements up to $l \sim 3000$.

Finally, we highlighted the physical differences between the Λ CDM power spectrum and those of other models through their ratio (i.e., the so-called boost), shown in Fig. 8 for the MEDIUMHR simulations. As hinted earlier, modified gravity setups (top panel) show a boost up to 15% in the MG-F5 model (at $l \sim 10^3$), with milder effects, albeit still of a few percent, in the MG-F6 case. Dark scattering models (bottom panels) show the opposite behavior that we already discussed in Section 3.1, due to the different signs of $A(z)$ (albeit with milder effects in the DS-THAW case). We omit the relative differences for boosts specifically, since they are essentially comparable to those of the beyond- Λ CDM models (Fig. 7).

3.3. Weak lensing convergence maps

We used the `dorian` Python package⁶ (Ferlito et al. 2024) to produce weak lensing convergence maps and power spectra from the sky-projected lightcone matter density maps. The code performs a weak gravitational lensing analysis through ray-tracing of a source at a certain redshift. Due to the resolution of our simulations, we are limited to $\text{NSIDE} = 1024$. While this is a low value for the standards of modern weak lensing analysis, we are still able to compute the convergence power spectrum and assess its accuracy with the DZS algorithm. We do so for the MEDIUMHR simulations, across two of our beyond- Λ CDM models. We anticipate that using a higher value of NSIDE , i.e., runs

⁶ <https://gitlab.mpcdf.mpg.de/fferlito/dorian>.

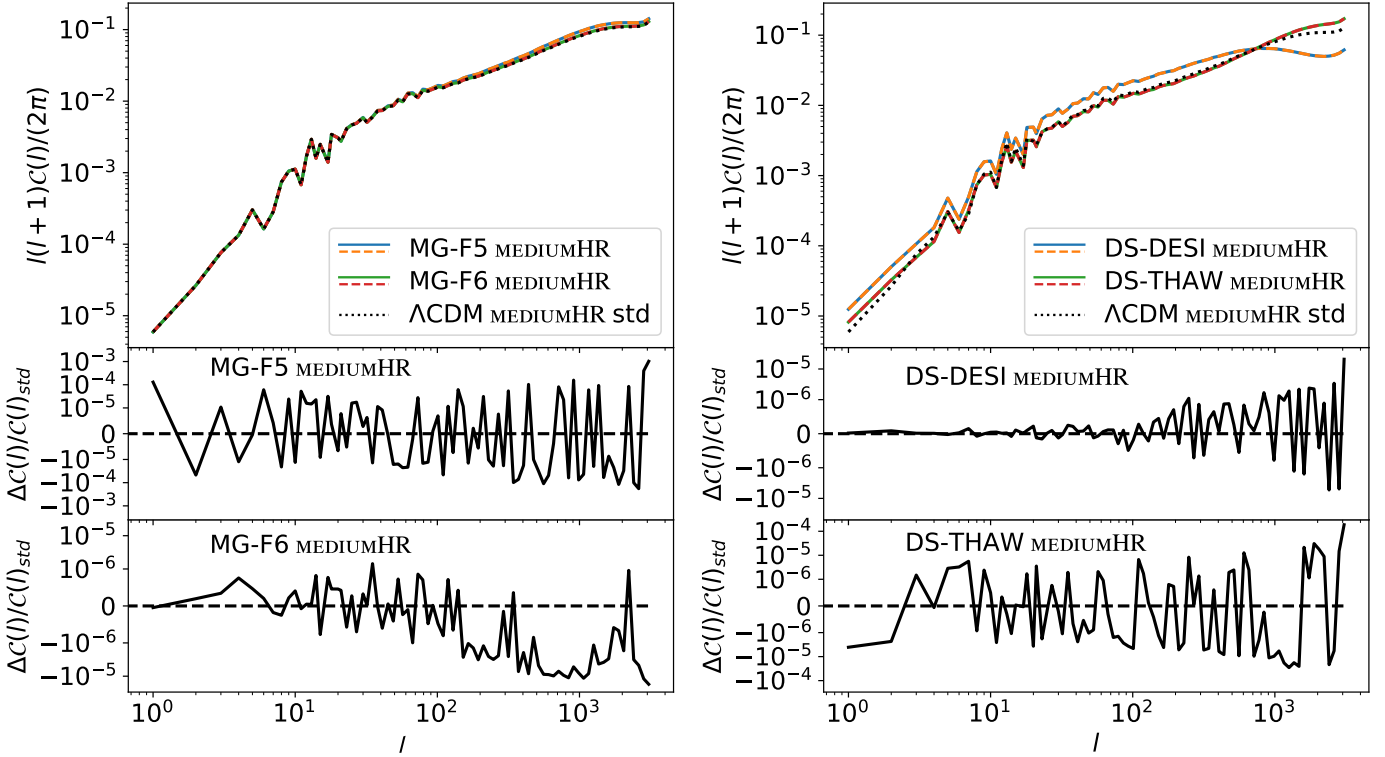


Fig. 7. Left column: Angular power spectrum $C(l)$ of the MG-Arepo MEDIUMHR simulations, for the MG-F5 and MG-F6 models (top panel). Solid lines refer to `std` runs, dashed lines to `dzs` ones. The Λ CDM `std` case (dotted line) is overlaid as a reference. Relative difference plots are included for both MG models (middle and bottom panels, as labeled), with a dashed line indicating $\Delta C(l) = 0$ for reference. Right column: The same as in the left column, but for the DS-DES/THAW MEDIUMHR simulations.

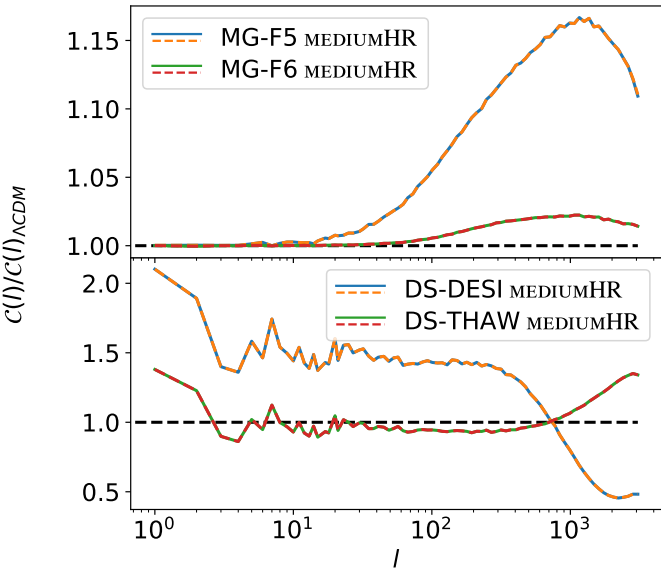


Fig. 8. Power spectrum boosts, i.e., the ratio $C(l)/C(l)_{\Lambda\text{CDM}}$, of the MEDIUMHR simulations, for MG models (top panel) and DS ones (bottom panel). Dashed lines at unit boost are shown for reference.

ning a higher-resolution simulation, could yield improved (or, at worst, similar) relative differences in convergence power spectra with respect to our $\text{NSIDE} = 1024$ results. This follows from the behavior observed in the matter power spectra at different resolutions (Figs. 7 and A.1).

Figure 9 shows the results of our analysis for the MG-F5 and DS-DES/THAW models. We note a $\leq 1\%$ accuracy across all the range of l for the former model and a 0.01% accuracy at worst for the latter one. We note that these results are orders of magnitude higher (in absolute value) than those of the corresponding matter power spectra (Fig. 7). In fact, the massmaps that give rise to the matter power spectrum are built through a pixel-wise sum of several individual ‘‘shells’’ (30, for the MEDIUMHR volume), each spanning a small redshift range to collectively cover $z \in [\sim 0.36, 0]$. This tends to smooth out differences in individual shells. The `dorian` code, on the other hand, goes through each shell sequentially, resulting in more significant differences. Nonetheless, we remark that the accuracy of the DZS method is high also for the weak lensing convergence power spectra, as it fits within the 1% requirement for Euclid mentioned in Section 3.2, and especially so in the DS-DES/THAW case.

3.4. Run time performance

In the previous sections, we have verified that the DZS algorithm is accurate in reproducing lightcone-like output. Now, we quantify how much computational time we are able to save in our validation suite across the different cosmologies examined. Table 3 shows the percentage of time saved by a `dzs` simulation with respect to the corresponding `std` run. The speedup, here defined as the total time taken by the `std` run divided by the `dzs` one, is shown in brackets. As expected, a larger volume yields higher computational time savings in every cosmological model. Moreover, a comparison between the `LARGE` and `LARGEHR` simulations reveals that an increased resolution results in a larger time saving. We expect this trend to persist when pushing for higher,

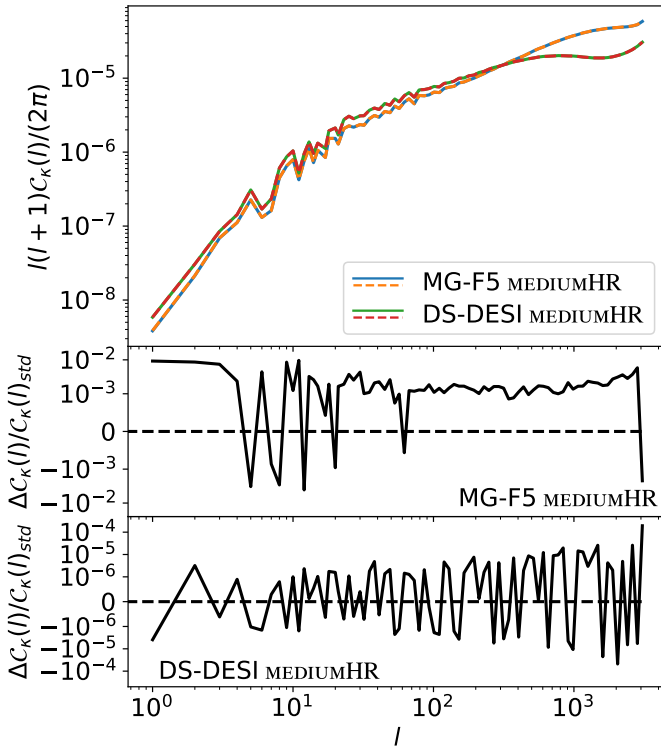


Fig. 9. Weak lensing convergence power spectrum $C_k(l)$ of the MEDIUMHR simulations, for the MG-F5 and DS-DESI models (top panel). Solid lines refer to std runs, dashed lines to dzs ones. Relative difference plots are included for both MG models (middle and bottom panels), with a dashed line at $\Delta C_k(l) = 0$ for reference.

state-of-the-art resolutions, enabling massive performance gains (see Section 4 for an approximate analysis on this aspect). This trend also appears in the smaller volumes simulated, albeit with the notable exceptions of the Λ CDM and MG-F6 models where the time saving in the MEDIUMHR setup is $\approx 1\%$ lower than that of the MEDIUM one. While we have run every simulation in our testing suite on computational units with identical hardware specifications, fluctuations among different units (and on the same unit at different times) are always present. Therefore, we ascribe the somewhat inconsistent trend in the smaller volume to machine fluctuations coupled with a relatively low impact of the DZS algorithm, which only operates at redshift $\lesssim 0.69$.

There are notable differences in performance also between different cosmological models. The best-performing model in every setup is MG-F5, for which we saved an impressive $\sim 53\%$ of the computing time in the LARGEHR simulations. This is expected, given the computationally demanding multi-grid technique employed to calculate MG effects, coupled with the high strength of the scalar field responsible for them. The performance of the multi-grid technique depends on the number of particles of a simulation, as well as their degree of clustering; therefore, by drastically reducing both the number of particles and their resolution, the DZS technique is able to yield a high performance gain in MG simulations. The presence of the same multi-grid technique, albeit with lower field strength, brings the MG-F6 to a close second place in terms of performance gain. Notably, as hinted above, the parameters on which the DZS algorithm depends can be tweaked to achieve better performance at the cost of accuracy, and vice versa. In principle, the MG setups could therefore be made more accurate – i.e., on par with the Λ CDM and DS-DESI models in Fig. 5 – by reducing their

performance gain, which would then also be on par with Λ CDM and DS-DESI results. Nonetheless, we note that the same DZS parameter choices lead to an inherently higher performance gain in MG models.

On the other hand, the DS setups show slightly lower performance gains than all of the other models. We speculate that this could be due to Gadget4 being harder to optimize than Arepo on some systems, somewhat hindering the achievable performance. In any case, the performance gain is up to 43% in all of the LARGE and LARGEHR simulations, and significant ($\lesssim 18\%$) also in the smaller setups (especially in MG models). We also note that DZS-related operations themselves (tree walk and particle addition/elimination) do not add any significant overhead, as the wall-clock time taken by them is always of the order $\sim 0.1\%$ of the total simulation time.

In addition to this run-time performance gain analysis, Appendix B details the workload balance of our validation suite, to see how DZS-related modifications to particle number and resolution affect the workload distribution between parallel tasks. In the case of imbalances in this distribution, further performance improvements could be achieved through dedicated optimization techniques.

4. High-resolution performance gain estimation

While the testing suite employed so far has proved that the DZS algorithm is able to boost the performance of large-scale simulations without significant accuracy losses, such a suite does not represent the state-of-the-art simulations that our method is targeted at. As mentioned previously, we needed computationally inexpensive simulations to thoroughly test our chosen cosmological models. Here, we provide an approximate estimate of the DZS performance gain at a more realistic resolution for produc-

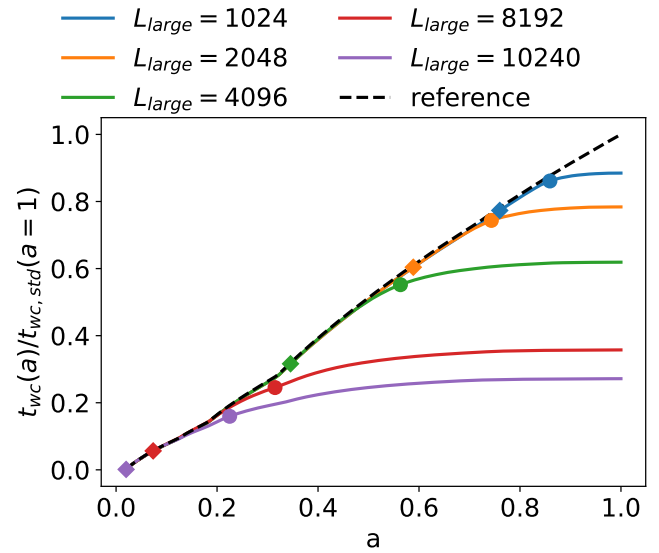


Fig. 10. Cumulative wall-clock times $t_{wc}(a)$ of each rescaled dzs run of the $L_{box} = 100 \text{ cMpc}/h$, $N_{part} = 512^3$ setup as a function of the scale factor a . The times are normalized to the final (total wall-clock) time of an std run with the same setup. The latter simulation is also included as a dashed black line for reference. The diamond symbol marks the time at which the rescaled lightcone enters the simulation volume and the DZS algorithm starts merging particles. The circular symbol shows when the number of particles becomes lower than half of the initial value as a result of the merging operation. The values of L_{large} are in cMpc/h .

Table 3. Percentage of run time saved by dzs relative to std runs, with the corresponding speedup (in brackets) for every examined combination of initial conditions (columns) and cosmological model (rows).

	MEDIUM	MEDIUMHR	LARGE	LARGEHR
Λ CDM	18.39% (1.23)	17.76% (1.22)	33.46% (1.50)	49.09% (1.96)
MG-F5	25.99% (1.35)	27.14% (1.37)	36.99% (1.59)	52.79% (2.12)
MG-F6	23.93% (1.31)	22.47% (1.29)	36.33% (1.57)	51.36% (2.06)
DS-DESI	8.68% (1.09)	18.17% (1.22)	29.14% (1.41)	43.24% (1.76)
DS-THAW	11.95% (1.14)	17.53% (1.21)	25.73% (1.35)	42.79% (1.75)

tion runs. Note that, due to the limited computational resources available, we carried out this analysis only for Λ CDM cosmology. We expect more expensive simulation setups (such as those performed with MG-Arepo) to yield a higher performance gain, as discussed in Section 3.4.

Our starting element in this analysis was a new simulation setup with $L_{box} = 100$ cMpc/h and $N_{part} = 512^3$, which corresponds to a mass resolution of $6.43 \times 10^8 M_\odot/h$ with the cosmological parameters adopted in this work. This resolution is comparable with e.g., the MillenniumTNG and Euclid flagships simulations, therefore we consider it representative of state-of-the-art, large-scale simulations. Since the small L_{box} value does not normally yield a significant DZS-related performance gain (as the lightcone would enter the volume at a redshift close to zero), we rescaled the real lightcone by a user-defined factor that mimics the evolution of $R_{lc}(z)$ in larger boxes with side L_{large} , such that $R_{lc,rescaled}(z) = R_{lc}(z)L_{box}/L_{large}$. We chose different values for L_{large} , namely 1024, 2048, 4096, 8192, and 10240 cMpc/h. We then compared the run times of dzs simulations employing $R_{lc,rescaled}$ with a reference std run. While such an approach yields a performance gain estimate for large-scale, high-resolution simulations, the use of a small L_{box} implies the absence of large-scale density fluctuations that significantly enhance the gravitational potential and, consequently, non-linearity and computational cost. On the other hand, a real state-of-the-art setup would require a massively parallel environment with tens (or hundreds) of thousands of simultaneous tasks, where workload imbalances arise as a result of DZS operations (see Appendix B). Nonetheless, we believe this to be an interesting and relatively inexpensive approach to assess the capabilities of our method in realistic setups.

Figure 10 shows the cumulative wall-clock time $t_{wc}(a)$ taken by each of the examined values of L_{large} , as well as by the reference run itself, as a function of the scale factor a . The values are normalized to the redshift-zero value of the reference simulation $t_{wc,std}(a = 1)$. First of all, we note that each curve (except the ‘‘reference’’ one) flattens after DZS has significantly reduced the number of particles in the simulation. Interestingly, a noticeable flattening is present also in the smallest $L_{large} = 1024$ cMpc/h, corresponding to a run time saving of 12%. As expected, larger volumes show increasingly better results, from 22% with $L_{large} = 2048$ cMpc/h to 64% and 73% in the largest rescalings of $L_{large} = 8192$ cMpc/h and 10240 cMpc/h, respectively. The latter case ideally translates into a flagship-like simulation, with unique lightcone output (i.e., without volume replications) available up to redshift ~ 4 , completed in just 1/4 of the time that it would normally take. Moreover, we note that our intermediate rescaled volume $L_{large} = 4096$ cMpc/h is only slightly larger than that of the Euclid flagships, and yields a run time saving of 38%. This suggests that a similar saving could be achieved by running those simulations with the DZS algorithm. Overall, these results imply that the DZS method can bring major performance improvements to state-of-the-art, large-scale simu-

lations, also enabling multiple simulations (with different cosmologies) in the time span normally taken by a single run.

Furthermore, the 2048 and 8192 cMpc/h rescalings enable a direct comparison with the Λ CDM results in Table 3: both the MEDIUM and MEDIUMHR simulations are slightly outperformed by $L_{large} = 2048$ cMpc/h. More noticeably, rescaling the high-resolution simulation to 8192 cMpc/h saves 30% more time than in the LARGE case, and 15% more time than in the LARGEHR. This agrees with the trend originally observed in Section 3.4; namely, increasing the resolution on a fixed volume also increases the run time saved thanks to the DZS method. Lastly, we note that rescaling to $L_{large} = 10240$ cMpc/h mimics a volume so large that it is not fully contained in the lightcone at the beginning of the simulation, allowing the DZS algorithm to redefine chunks of that volume right away on the first timestep.

5. Summary and conclusions

In this paper, we presented implementations of the Dynamic Zoom Simulations (DZS) algorithm in the massively parallel codes for N-body simulations Arepo and Gadget4 across different cosmological models. DZS substantially improves the performance of large-scale cosmological simulations that produce a lightcone-like output, with minimal impact on the accuracy of the results. This performance improvement is achieved by focusing computational resources inside the lightcone by reducing the simulation resolution outside of it. The algorithm is also fully compatible with the gravitational treePM solver widely adopted in state-of-the-art codes, and requires only minimal modifications to their workflow. In fact, this high degree of compatibility allows the algorithm to work even in non-standard cosmologies, like modified gravity (modeled in the code MG-Arepo through a computationally expensive multi-grid solver) and dynamic dark energy models (in the code PANDA-Gadget4), making it a very powerful performance-enhancing tool for constraining such models.

Enabling and validating the DZS approach in these beyond- Λ CDM codes yielded the following results:

- simulations performed with the DZS algorithm complete in significantly less time relative to their standard counterparts: in our testing setups, a large cubic volume 8192 cMpc/h on a side yields a run time saving of up to $\sim 50\%$. We also tested a smaller volume 2048 cMpc/h on a side, which still enables a saving of up to $\sim 25\%$ (Table 3). The volume size correlates with the performance gain, since the lightcone crosses larger volumes sooner.
- Other than the volume size, employing different cosmological models also affects the performance. In general, more computationally expensive cosmological models yield higher DZS-related performance gains (Table 3). For instance, modified $f(R)$ gravity setups lead to up to $\sim 10\%$ more computing time savings than Λ CDM or dark scattering simulations.

- By comparing lightcone-like output from the same simulations performed with and without DZS, we assessed the accuracy of the algorithm in reproducing such output. Relative differences in the lightcone halo mass function (Figs. 3 and 4), sky-projected massmaps (Fig. 5), and angular power spectra of matter (Figs. 6 and 7, and Figs. A.1 and A.2 in Appendix A) and weak lensing convergence (Fig. 9) are typically of order 0.1% or lower. Boost and deboosts in the matter power spectra due to non-standard effects are also accurately reproduced by the DZS algorithm (Fig. 8), on a level comparable with that of the power spectra themselves and, for example, well below the 1% value discussed in [Euclid Collaboration \(2025a\)](#).
- Our tests suggest that higher resolution leads to larger time savings, due to the more accurate, and therefore more computationally expensive, depiction of non-linear matter clustering effects (Table 3). To estimate the performance gain in large-scale simulations with state-of-the-art resolutions we simulated a small volume at a much higher resolution than our default test setups, and approximated the effects of the DZS algorithm in large boxes through a rescaling of the lightcone. This approach predicted run time savings of $\sim 65\%$ with a 8192 cMpc/h box (Fig. 10), in agreement with the trend of our validation setups. This result improves up to an impressive $\sim 75\%$ wall-clock time reduction for a larger 10240 cMpc/h box.

In conclusion, our implementation and validation work suggests that DZS is a very valuable tool to address the technical challenges of the next generation of cosmological simulations. In particular, this technique enables a computationally cost-effective way to thoroughly constrain the unprecedented amount of data from current and upcoming surveys, across multiple cosmological models.

Acknowledgements. We are very grateful to everyone that made this work possible. We thank Volker Springel for granting access to the developer version of Arepo, as well as providing extensive explanations and support on specific parts of the code. We also thank Baojiu Li, Christian Arnold and César Hernández Aguayo for allowing us to use MG-Arepo in our analysis. We acknowledge the Open Physics Hub project (hosted by the University of Bologna) for granting us access to their computational resources. We also gratefully acknowledge the Gauss Centre for Supercomputing e.V. (www.gauss-centre.eu) for funding this project by providing computing time on the GCS Supercomputer SuperMUC-NG at Leibniz Supercomputing Centre (www.lrz.de). In addition, we acknowledge the EuroHPC Joint Undertaking for awarding this project access to the EuroHPC supercomputer LUMI, hosted by CSC (Finland) and the LUMI consortium, through EuroHPC Development and Benchmark Access calls. We are grateful to Fulvio Ferlito for providing active and extensive support for the dorian package. RZ is funded by the European Union - NextGenerationEU, National Recovery and Resilience Plan (NRRP), Mission 4, Component 2, CUP J33C23002460002. EG is supported by the Kakenhi 23K20035 grant. Finally, we thank the developers and maintainers of other python packages used in this work, namely `numpy` ([Van Der Walt et al. 2011](#)), `scipy` ([Virtanen et al. 2020](#)), `h5py` ([Collette 2013](#)), `matplotlib` ([Hunter 2007](#)), `healpy` ([Zonca et al. 2019](#)) and `ligo.skymap` ([Singer & Price 2016](#); [Singer et al. 2016](#)).

Barnes, J. & Hut, P. 1986, *Nature*, 324, 446
 Berlind, A. A. & Weinberg, D. H. 2002, *ApJ*, 575, 587
 Bode, P., Ostriker, J. P., & Xu, G. 2000, *ApJS*, 128, 561
 Braun, R., Bourke, T., Green, J. A., Keane, E., & Wagg, J. 2015, in *Advancing Astrophysics with the Square Kilometre Array (AASKA14)*, 174
 Carroll, S. M., Hoffman, M., & Trodden, M. 2003, *Phys. Rev. D*, 68, 023509
 Chisari, N. E. & Zaldarriaga, M. 2011, *Phys. Rev. D*, 83, 123505
 Collette, A. 2013, *Python and HDF5* (O'Reilly)
 Conroy, C., Wechsler, R. H., & Kravtsov, A. V. 2006, *ApJ*, 647, 201
 Cruickshank, N., Crittenden, R., Koyama, K., & Bruni, M. 2025, *J. Cosmology Astropart. Phys.*, 2025, 052
 Davis, M., Efstathiou, G., Frenk, C. S., & White, S. D. M. 1985, *ApJ*, 292, 371
 DESI Collaboration, Aghamousa, A., Aguilar, J., et al. 2016a, arXiv e-prints, arXiv:1611.00036
 DESI Collaboration, Aghamousa, A., Aguilar, J., et al. 2016b, arXiv e-prints, arXiv:1611.00037
 Euclid Collaboration, Adamek, J., Fiorini, B., et al. 2025a, *A&A*, 695, A230
 Euclid Collaboration, Blanchard, A., Camera, S., et al. 2020, *A&A*, 642, A191
 Euclid Collaboration, Castander, F. J., Fosalba, P., et al. 2025b, *A&A*, 697, A5
 Euclid Collaboration, Mellier, Y., Abdurro'uf, et al. 2025c, *A&A*, 697, A1
 Evrard, A. E., MacFarland, T. J., Couchman, H. M. P., et al. 2002, *ApJ*, 573, 7
 Farrar, G. R. & Peebles, P. J. E. 2004, *ApJ*, 604, 1
 Ferlito, F., Davies, C. T., Springel, V., et al. 2024, *MNRAS*, 533, 3209
 Fosalba, P., Gaztañaga, E., Castander, F. J., & Manera, M. 2008, *MNRAS*, 391, 435
 Garaldi, E., Nori, M., & Baldi, M. 2020, *MNRAS*, 499, 2685
 Górski, K. M., Hivon, E., Banday, A. J., et al. 2005, *ApJ*, 622, 759
 Hagstotz, S., Costanzi, M., Baldi, M., & Weller, J. 2019, *MNRAS*, 486, 3927
 Hahn, O. & Abel, T. 2011, *MNRAS*, 415, 2101
 Henriques, B. M. B., White, S. D. M., Thomas, P. A., et al. 2015, *MNRAS*, 451, 2663
 Hirschmann, M., De Lucia, G., & Fontanot, F. 2016, *MNRAS*, 461, 1760
 Hu, W. & Sawicki, I. 2007, *Phys. Rev. D*, 76, 064004
 Hunter, J. D. 2007, *Computing in Science and Engineering*, 9, 90
 Ivezić, Ž., Kahn, S. M., Tyson, J. A., et al. 2019, *ApJ*, 873, 111
 Klypin, A. A. & Shandarin, S. F. 1983, *MNRAS*, 204, 891
 Lacey, C. G., Baugh, C. M., Frenk, C. S., et al. 2016, *MNRAS*, 462, 3854
 Laureijs, R., Amiaux, J., Arduini, S., et al. 2011, arXiv e-prints, arXiv:1110.3193
 Llinares, C. 2017, arXiv e-prints, arXiv:1709.04703
 Lodha, K., Calderon, R., Matthewson, W. L., et al. 2025, *Phys. Rev. D*, 112, 083511
 Message Passing Interface Forum. 1993, in *Supercomputing '93: Proceedings of the 1993 ACM/IEEE Conference on Supercomputing*, 878–883
 Nandra, K., Barret, D., Barcons, X., et al. 2013, arXiv e-prints, arXiv:1306.2307
 Nelson, D., Springel, V., Pillepich, A., et al. 2019, *Computational Astrophysics and Cosmology*, 6, 2
 Oyaizu, H. 2008, *Phys. Rev. D*, 78, 123523
 Pakmor, R., Springel, V., Coles, J. P., et al. 2023, *MNRAS*, 524, 2539
 Planck Collaboration, Aghanim, N., Akrami, Y., et al. 2020, *A&A*, 641, A6
 Potter, D., Stadel, J., & Teyssier, R. 2017, *Computational Astrophysics and Cosmology*, 4, 2
 Pourtsidou, A. & Tram, T. 2016, *Phys. Rev. D*, 94, 043518
 Primack, J. R. 2024, *Annual Review of Nuclear and Particle Science*, 74, 173
 Puchwein, E., Baldi, M., & Springel, V. 2013, *MNRAS*, 436, 348
 Simpson, F. 2010, *Phys. Rev. D*, 82, 083505
 Singer, L. P., Chen, H.-Y., Holz, D. E., et al. 2016, *ApJ*, 829, L15
 Singer, L. P. & Price, L. R. 2016, *Phys. Rev. D*, 93, 024013
 Somerville, R. S. & Davé, R. 2015, *ARA&A*, 53, 51
 Somerville, R. S., Popping, G., & Trager, S. C. 2015, *MNRAS*, 453, 4337
 Spergel, D., Gehrels, N., Baltay, C., et al. 2015, arXiv e-prints, arXiv:1503.03757
 Springel, V. 2005, *MNRAS*, 364, 1105
 Springel, V. 2010, *MNRAS*, 401, 791
 Springel, V. 2012, *Astronomische Nachrichten*, 333, 515
 Springel, V., Pakmor, R., Zier, O., & Reinecke, M. 2021, *MNRAS*, 506, 2871
 Van Der Walt, S., Colbert, S. C., & Varoquaux, G. 2011, *Computing in Science and Engineering*, 13, 22
 Vikman, A. 2005, *Phys. Rev. D*, 71, 023515
 Virtanen, P., Gommers, R., Oliphant, T. E., et al. 2020, *Nature Medicine*, 17, 261
 Vogelsberger, M., Marinacci, F., Torrey, P., & Puchwein, E. 2020, *Nature Reviews Physics*, 2, 42
 Weinberger, R., Springel, V., & Pakmor, R. 2020, *ApJS*, 248, 32
 Wetterich, C. 1995, *A&A*, 301, 321
 Will, C. M. 2014, *Living Reviews in Relativity*, 17, 4
 Winther, H. A., Schmidt, F., Barreira, A., et al. 2015, *MNRAS*, 454, 4208
 Xu, G. 1995, *ApJS*, 98, 355
 Zonca, A., Singer, L., Lenz, D., et al. 2019, *The Journal of Open Source Software*, 4, 1298

References

Abdul Karim, M., Aguilar, J., Ahlen, S., et al. 2025, *Phys. Rev. D*, 112, 083515
 Alimi, J.-M., Bouillot, V., Rasera, Y., et al. 2012, arXiv e-prints, arXiv:1206.2838
 Amendola, L. 2000, *Phys. Rev. D*, 62, 043511
 Angulo, R. E. & Hahn, O. 2022, *Living Reviews in Computational Astrophysics*, 8, 1
 Angulo, R. E., Springel, V., White, S. D. M., et al. 2012, *MNRAS*, 426, 2046
 Arnold, C., Leo, M., & Li, B. 2019, *Nature Astronomy*, 3, 945
 Bagla, J. S. 2002, *Journal of Astrophysics and Astronomy*, 23, 185
 Baldi, M. & Simpson, F. 2015, *MNRAS*, 449, 2239
 Baldi, M. & Simpson, F. 2017, *MNRAS*, 465, 653

Appendix A: Angular matter power spectra of additional non-standard simulations

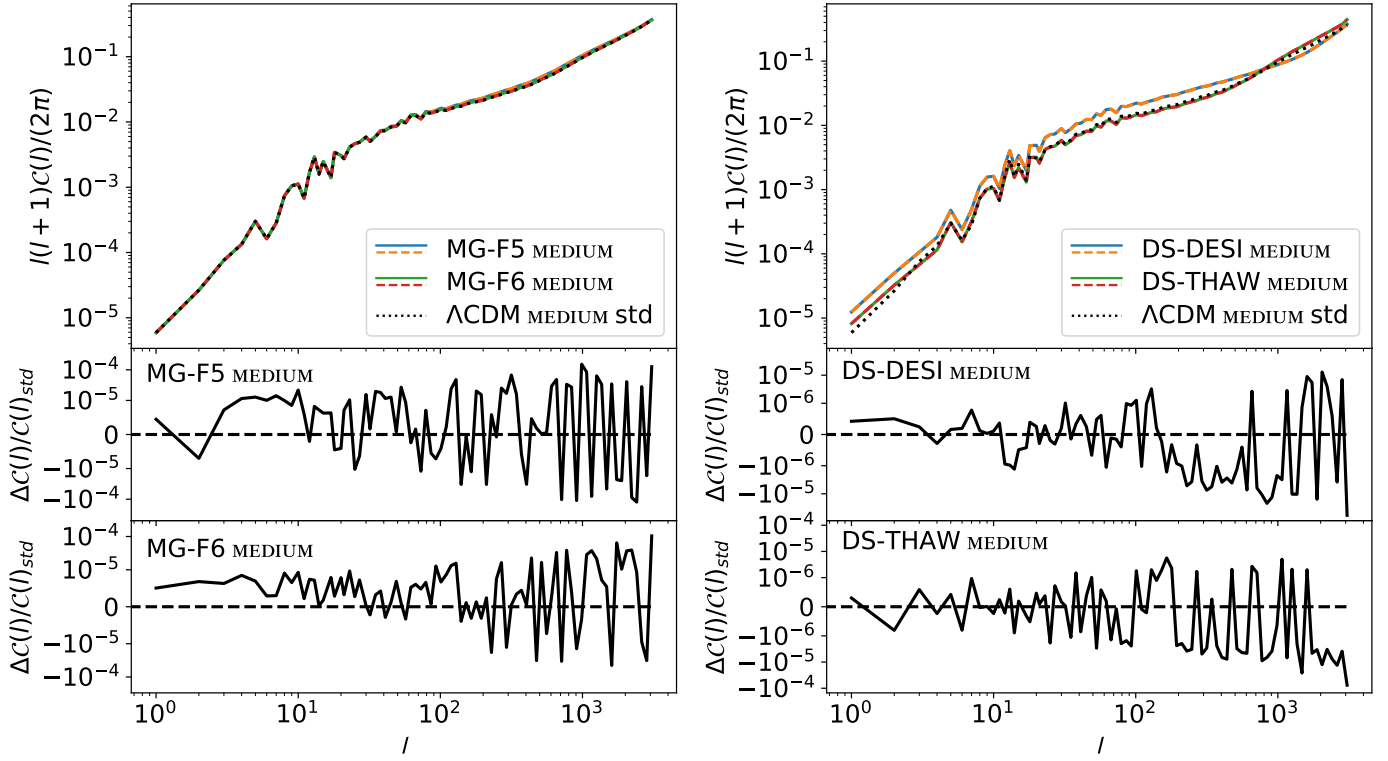


Fig. A.1. *Left column:* Angular power spectrum $C(l)$ of the MG-Arepo MEDIUM simulations, for the MG-F5 and MG-F6 models (top panel). Solid lines refer to std runs, dashed lines to dzs ones. The Λ CDM std case (dotted line) is overlaid as a reference. Relative difference plots are included for both MG models (middle and bottom panels, as labeled), with a dashed line indicating $\Delta C(l) = 0$ for reference. *Right column:* The same as in the left column, but for the DS-DESI and DS-THAW MEDIUM simulations.

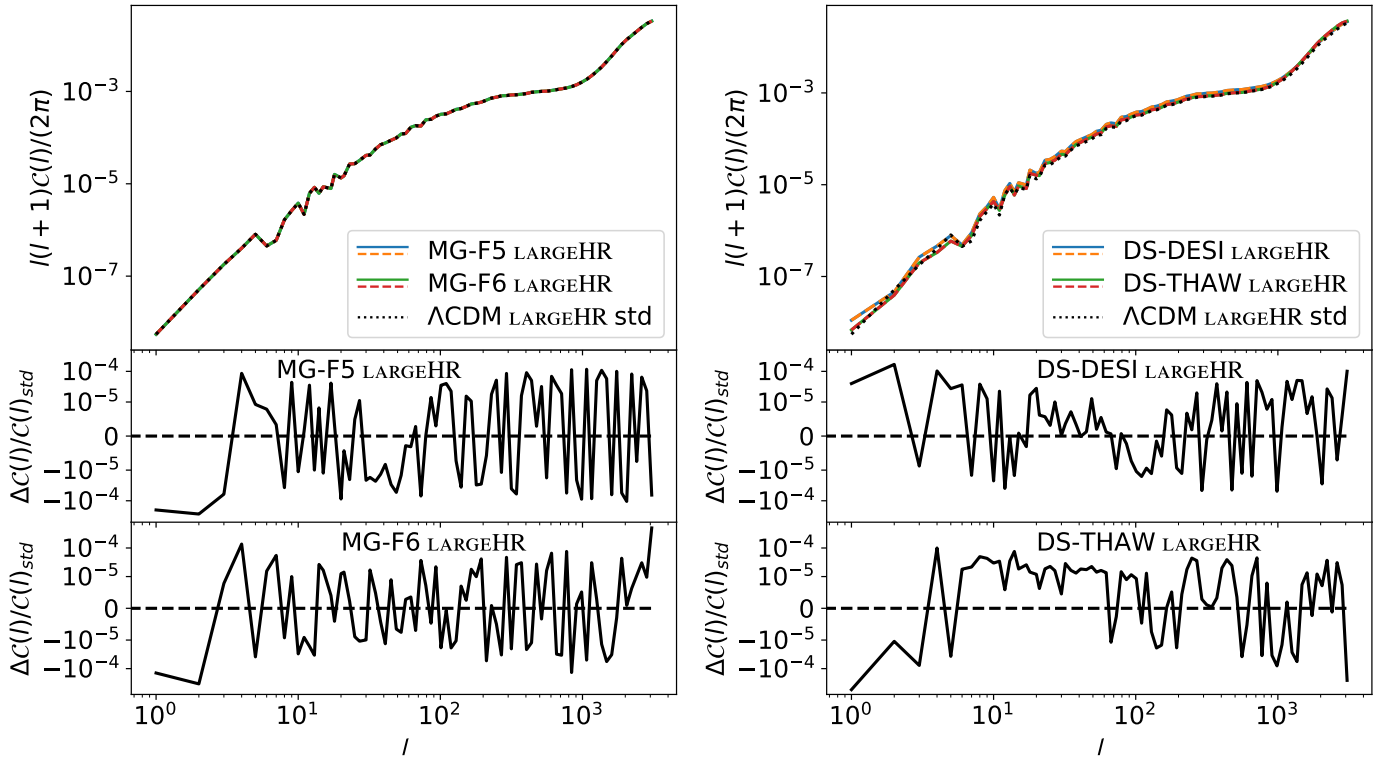


Fig. A.2. Same as in Fig. A.1, but for the LARGEHR simulations.

In this Appendix, we present angular matter power spectra from the beyond- Λ CDM MEDIUM and LARGEHR simulations, in Figs. A.1 and A.2, respectively. As in the MEDIUMHR and Λ CDM simulations described in Section 3.2, relative differences between dzs and std simulations remain very small, never exceeding $\sim 0.01\%$. Non-standard features are still recognizable with respect to the reference standard model (dotted black line), especially in the MEDIUM setups (thanks to the narrower redshift range where output is produced). Even though a comparison between Figs. 7 and A.1 reveals that the accuracy does not always increase with increasing resolution (as already noted in Section 3.2) these additional results remark the very high accuracy yielded by the DZS algorithm, across the different setups and models of our validation suite.

Appendix B: Workload balance

While the DZS-induced performance gain observed in Section 3.4 is significant, we assessed if there is room for further improvement, by checking how the workload balance⁷ changes when the DZS algorithm is operating. Indeed, we expect that the presence of multiple resolutions in a simulation, as well as the overall smaller number of particles, will make it more difficult to evenly distribute the work and particle load among parallel tasks.

Figure B.1 shows the workload balance as a function of the scale factor a for all Λ CDM twin simulations, with solid lines referring to std runs and dashed lines to dzs ones. From the moment in which the lightcone enters the simulation volume (indicated by the diamond marker in Fig. B.1) and the DZS algorithm starts to merge particles, the balance in dzs runs diverges from the ideal value of 1, going as high as ~ 1.1 in the MEDIUMHR and LARGEHR simulations. The effect is especially prominent after the number of particles in DZS drops below half of the initial value (a time marked by the circle in the figure). While there is still room for improvement, for example through appropriate weighting in the domain decomposition or a change in the number of computing tasks mid-simulation (the so-called “DZS special stop” in Garaldi et al. 2020), this result represents only a slight imbalance. In fact, part of the observed imbalance could also be caused by machine fluctuations, as in the case of the LARGE simulations, where the balance lies noticeably above the ideal value also in the std run.

The workload balance for beyond- Λ CDM models is shown in Fig. B.2. The lower resolution MG setups, that is, the MEDIUM and LARGE runs in the left column of the figure, behave relatively well, with peaks up to ~ 1.5 in the dzs MG-F6 MEDIUM simulation. Their higher-resolution counterparts, however, peak at values of 2 or even 3, as in the case of the MG-F5 MEDIUMHR setup. While such values are limited to a handful of timesteps, they will need to be thoroughly investigated to improve the performance of DZS in modified gravity setups. We leave such an investigation to a potential follow-up analysis, as the observed run time saving is already satisfactory ($\gtrsim 50\%$ in the largest volume). Dark scattering simulations (right column of Fig. B.2) align with the lower-resolution MG setups, with dzs runs going as high as ~ 1.5 in workload balance. In fact, the most prominent feature arising in DS runs (both std and dzs) is the very narrow spikes resulting from the use, in Gadget4, of the

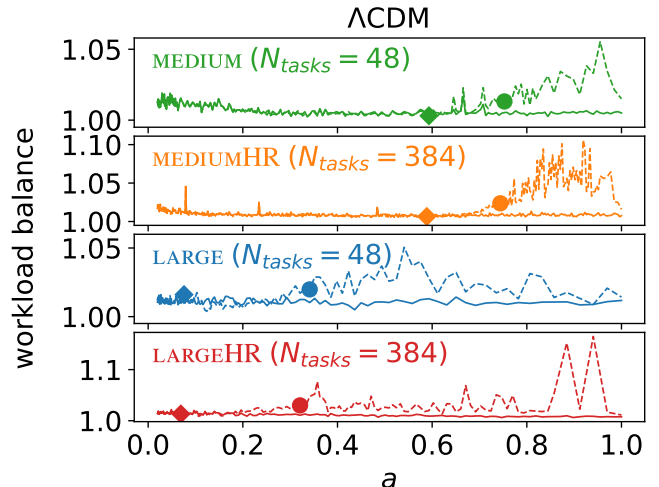


Fig. B.1. Workload balance for all the Λ CDM simulations performed in this work as a function of the scale factor a . The number of parallel tasks N_{tasks} is included for each setup. Solid lines refer to std runs, dashed lines to dzs ones. The diamond symbol marks the time at which the lightcone enters the simulation volume and the DZS algorithm starts merging particles. The circular symbol shows when the number of particles becomes lower than half of the initial value as a result of the merging operation.

hybrid shared-distributed memory variant of MPI mentioned in 2.2. Normally, each parallel MPI task is assigned its own memory and needs to communicate with other tasks to exchange contents of that memory. Conversely, Gadget4 uses a version of MPI where memory is shared within tasks on the same node (mirroring the real, physical structure of individual computing nodes), and explicit communications are performed only between two or more nodes. This reduces memory overhead, but also introduces potential race conditions and inconsistent ordering of operations performed by different tasks. These break binary invariance of multiple reruns, which would hinder the accuracy tests performed in Section 3. Gadget4 allows to retain the invariance by forcing tasks to wait for others to access shared memory first, introducing sudden and temporary imbalances in the workload. Nonetheless, the DZS-induced gradual imbalance is still clearly recognizable. In conclusion, in both the MG and DS models, the DZS algorithm yields significant workload imbalances, which call for dedicated optimization techniques to be kept in check. We note that lowering the workload imbalance could potentially lead to even larger performance gains than those reported in Table 3.

⁷ The workload balance provides an estimate of how well the work is distributed between parallel computing tasks. For each timestep, it is defined as the maximum time, among all tasks, taken to evaluate tree gravitational interactions, divided by the average value.

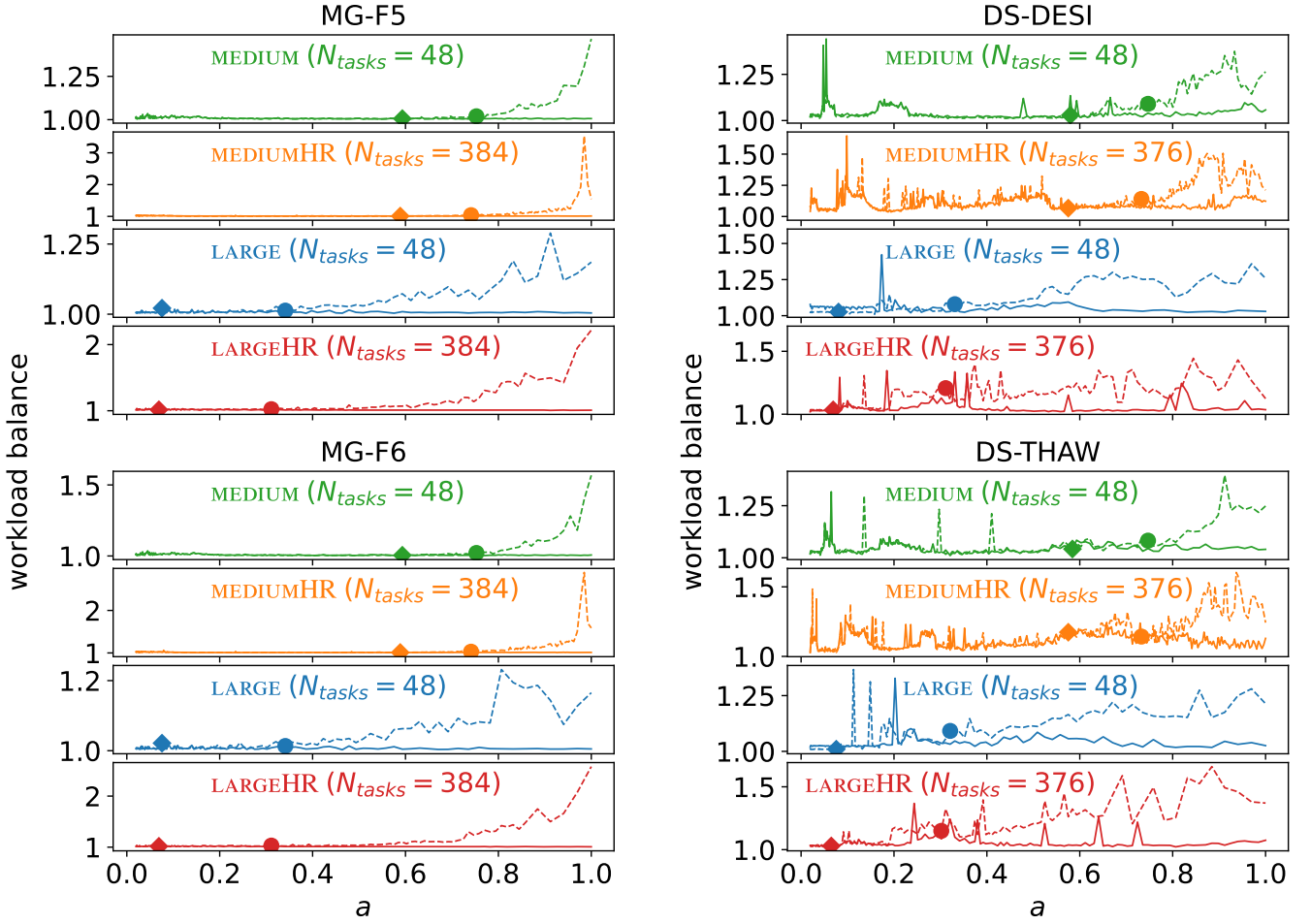


Fig. B.2. *Left column:* workload balance of all of the the MG-F5 (top) and MG-F6 (bottom) simulations tested as a function of the scale factor a . Solid lines refer to std runs, dashed lines to dzs ones. The number of parallel tasks N_{tasks} is included for each setup. The diamond symbol marks the time at which the lightcone enters the simulation volume and the DZS algorithm starts merging particles. The circular symbol shows when the number of particles becomes lower than half of the initial value as a result of the merging operation. *Right column:* the same as in the left column, but for the DS-DESI and DS-THAW simulations.